remote sensing

MDPI

Article

Wildfire Smoke Particle Properties and Evolution, From Space-Based Multi-Angle Imaging II: The Williams Flats Fire during the FIREX-AQ Campaign

Katherine T. Junghenn Noyes [1,*], Ralph A. Kahn [1,2], James A. Limbacher [2,3], Zhanqing Li [1,4], Marta A. Fenn [5,6], David M. Giles [2,7], Johnathan W. Hair [5], Joseph M. Katich [8,9], Richard H. Moore [5], Claire E. Robinson [5,6], Kevin J. Sanchez [5,10], Taylor J. Shingler [5], Kenneth L. Thornhill [5,6], Elizabeth B. Wiggins [5,10] and Edward L. Winstead [5,6]

1 Department of Atmospheric and Oceanic Science, University of Maryland, College Park, MD 20742, USA; ralph.a.kahn@nasa.gov (R.A.K.); zhanqing@umd.edu (Z.L.)
2 NASA Goddard Space Flight Center, Greenbelt, MD 20771, USA; james.limbacher@nasa.gov (J.A.L.); david.m.giles@nasa.gov (D.M.G.)
3 Department of Meteorology and Atmospheric Science, The Pennsylvania State University, State College, PA 168026, USA
4 Earth System Science Interdisciplinary Center, College Park, MD 20740, USA
5 NASA Langley Research Center, Hampton, VA 23681, USA; marta.a.fenn@nasa.gov (M.A.F.); johnathan.w.hair@nasa.gov (J.W.H.); richard.h.moore@nasa.gov (R.H.M.); claire.e.robinson@nasa.gov (C.E.R.); kevin.j.sanchez@nasa.gov (K.J.S.); taylor.j.shingler@nasa.gov (T.J.S.); kenneth.l.thornhill@nasa.gov (K.L.T.); elizabeth.b.wiggins@nasa.gov (E.B.W.); edward.l.winstead@nasa.gov (E.L.W.)
6 Science Systems and Applications, Inc., Hampton, VA 23666, USA
7 Science Systems and Applications, Inc., Lanham, MD 20706, USA
8 Chemical Sciences Laboratory, NOAA Earth System Research Laboratories, Boulder, CO 80305, USA; joseph.m.katich@noaa.gov
9 Cooperative Institute for Research in Environmental Sciences (CIRES), University of Colorado Boulder, Boulder, CO 80309, USA
10 NASA Postdoctoral Program, Universities Space Research Association, Columbia, MD 21046, USA
* Correspondence: junghenn@umd.edu

Received: 28 October 2020; Accepted: 18 November 2020; Published: 21 November 2020

Abstract: Although the characteristics of biomass burning events and the ambient ecosystem determine emitted smoke composition, the conditions that modulate the partitioning of black carbon (BC) and brown carbon (BrC) formation are not well understood, nor are the spatial or temporal frequency of factors driving smoke particle evolution, such as hydration, coagulation, and oxidation, all of which impact smoke radiative forcing. In situ data from surface observation sites and aircraft field campaigns offer deep insight into the optical, chemical, and microphysical traits of biomass burning (BB) smoke aerosols, such as single scattering albedo (SSA) and size distribution, but cannot by themselves provide robust statistical characterization of both emitted and evolved particles. Data from the NASA Earth Observing System's Multi-Angle Imaging SpectroRadiometer (MISR) instrument can provide at least a partial picture of BB particle properties and their evolution downwind, once properly validated. Here we use in situ data from the joint NOAA/NASA 2019 Fire Influence on Regional to Global Environments Experiment-Air Quality (FIREX-AQ) field campaign to assess the strengths and limitations of MISR-derived constraints on particle size, shape, light-absorption, and its spectral slope, as well as plume height and associated wind vectors. Based on the satellite observations, we also offer inferences about aging mechanisms effecting downwind particle evolution, such as gravitational settling, oxidation, secondary particle formation, and the combination of particle aggregation and

condensational growth. This work builds upon our previous study, adding confidence to our interpretation of the remote-sensing data based on an expanded suite of in situ measurements for validation. The satellite and in situ measurements offer similar characterizations of particle property evolution as a function of smoke age for the 06 August Williams Flats Fire, and most of the key differences in particle size and absorption can be attributed to differences in sampling and changes in the plume geometry between sampling times. Whereas the aircraft data provide validation for the MISR retrievals, the satellite data offer a spatially continuous mapping of particle properties over the plume, which helps identify trends in particle property downwind evolution that are ambiguous in the sparsely sampled aircraft transects. The MISR data record is more than two decades long, offering future opportunities to study regional wildfire plume behavior statistically, where aircraft data are limited or entirely lacking.

Keywords: biomass burning; remote sensing; MISR; smoke plume; particle properties; aerosols; FIREX-AQ; wildfire; plume heights

1. Introduction

Wildfire smoke emissions are a rich and complex mixture of gas and aerosol constituents, the impacts of which occur over wide temporal and spatial scales and can result in short-term regional air quality issues as well as climate forcing. Globally, wildfires are the most significant source of light-absorbing black carbon (BC) and brown carbon (BrC) airborne particles [1,2]; they can also be considerable sources of scattering aerosols and weakly absorbing soil or dust particles. The emission of all such particles can have broad consequences, many of which are interdependent and are not entirely understood at present. Light-absorbing aerosols can affect the local radiative budget by warming the surrounding air layer, in turn impacting atmospheric stability and potentially leading to changes in cloud distribution [3]. If they escape the planetary boundary layer (PBL), smoke particles can stay aloft for several days or more and be transported long distances, extending their radiative impact in both time and space [4,5]. As such, they may further impact cloud formation and lifetime, serving as cloud condensation nuclei (CCN) or, conversely, contributing to droplet warming and evaporation [3,6–8].

Emitted smoke composition varies widely between wildfires, and even over time for a single fire, with evidence suggesting there are systemic differences in particle size distribution, particle light absorption, and the spectral dependence of absorption based on the fuel type, fuel amount, burning characteristics, and meteorology [9–12]. For example, studies have suggested a connection between combustion efficiency (CE) and particle size at the point of emission, with smoldering fires (lower CE) generating larger particles than flaming fires (higher CE) under many conditions [13,14]. Fire regime has also been linked to smoke particle type—although BC is often the dominant absorbing aerosol in biomass burning (BB) smoke, smoldering fires tend to produce higher fractions of BrC than flaming ones [15–17]. In addition to exhibiting distinct chemical properties, BC and BrC are also optically unique in that BC is highly absorbing across all visible wavelengths, whereas BrC is less absorbing overall and displays enhanced absorption at shorter wavelengths [18,19]. These and other suggested differences in particle optical and physical properties indicate that the impacts of wildfires can vary over a wide range. However, the conditions that mediate these differences at the point of emission are not well understood. Furthermore, the microphysical properties and mixing state of BB particles can change dramatically even a short distance away from the source, as aerosols interact with water vapor, trace gases, and other particles through a variety of complex processes. For example, as smoke cools away from the flame front, semi-volatile gases (known as volatile organic compounds, or VOCs) can condense onto existing emitted particles, creating organic or inorganic coatings that result in increased particle size, particle scattering, and CCN efficiency, especially in the case of BC (which is hydrophobic in its pure form) [14,20–24]. VOCs can also spontaneously condense into new,

very small particles, a process known as secondary organic aerosol (SOA) formation, which increases the plume particle number concentration and shifts the particle size distribution to reflect smaller average diameters [23,25]. (In the atmospheric chemistry community, SOA formation is considered to include both new particle formation and VOC condensation onto existing particles. Here, we consider them as distinct aging mechanisms; from a remote sensing perspective, condensation on existing particles is usually classified as particle growth rather than new particle formation, especially as we often cannot distinguish the condensation of volatile organic gases from hygroscopic growth.) Organic aerosol (OA) has also been known to evaporate, transitioning from the particle to the gas phase [26]. These processes often occur in combinations that may change on relatively short temporal and spatial scales.

As wildfire frequency and severity are expected to increase with global warming, it is becoming increasingly important to improve our understanding of the factors controlling wildfire smoke particle properties. In recent years, significant efforts have been made in this vein both in the laboratory (e.g., [20]) and in aircraft-based field campaigns (e.g., [27–29]). These experiments are able to observe plume gas- and particle-phase chemistry in great detail, and in some cases, can directly measure different aerosol types [30–32]. However, such experiments are unable to observe an entire plume in context, and they provide only a small set of BB cases, limiting their usefulness for robust statistical characterization of BB particle properties.

Satellite remote sensing data allows for snapshots of complete plumes and their surroundings. However, satellite instruments are unable to capture the fine detail that can be observed in situ, and in the past, have not provided ample constraints on key aerosol properties such as size and light-absorption. Early work was largely dedicated to retrieving the optical depth of ultraviolet (UV)-absorbing species, with substantial uncertainties due to the sensitivity of the results to the vertical distribution of the smoke and the contributions from other species [33,34]. To date, most chemical transport and climate models do not discriminate between BC and BrC, despite their distinct optical and physical properties, which therefore yield different environmental consequences [2,19]. Better characterization of fire-generated particles is thus a pressing issue for many modeling efforts.

Recently developed techniques allow for better characterization of previously unconstrained wildfire plume heights and particle properties from space, with the potential to improve our understanding of BB particles globally. These satellite products will achieve their greatest value when applied broadly, to numerous cases over entire ecosystems, yielding statistically robust patterns of smoke-plume behavior. However, the application of new satellite remote sensing techniques requires thorough validation against coincident in situ observations. Our previous work, (Junghenn-Noyes et al., 2020 [35], henceforth Paper 1) represents the first part of this program. It compares the height and particle property results and interpretations from NASA Earth Observing System's Multi-Angle Imaging Spectrometer (MISR) instrument with detailed, near-coincident aircraft observations of three wildfire smoke plumes during the U.S. Department of Energy's 2013 Biomass Burning Observation Project (BBOP) field campaign [27,28]. The current paper is Part 2 of this validation effort, comparing the satellite data with coincident DC-8 aircraft measurements made during the 2019 NASA-NOAA Fire Influence on Regional to Global Environments Experiment-Air Quality (FIREX-AQ) field campaign. Aside from the BBOP plumes, the 06 August 2019 Williams Flats fire plume studied here is nearly the only other existing case for which we have near-coincident MISR and detailed in situ chemical observations. The validation study presented here aims to place the satellite-retrieved plume particle characteristics on firmer ground, expanding the validation sample size and augmenting the validation effort in Paper 1. Although most of the aircraft instrument types used in FIREX-AQ are similar to those employed during BBOP, many of the instrument teams are different, and the FIREX-AQ campaign offered several additional validation resources, such as plume height, particle non-sphericity, and other lidar-retrieved measurements; the degree of flaming and smoldering measurements in the fire itself; and improved data on fuel type at the point of burning. These additions improve our previous understanding of MISR's ability to characterize wildfire plumes, compared to Paper 1, and

provide further insight into the relationships between measurements made by field scientists and the optical retrievals from satellites. The results from the combined validation studies set the stage for future work in developing a global climatology of BB aerosol plume properties and processes, which requires analyzing a broad, statistical sampling of MISR plume retrievals that are not also constrained by field observations. The current paper also highlights how a combined satellite–in situ approach is a superior method of observing wildfire smoke plumes during field campaigns.

Data sources and analysis methods are outlined in Section 2. Section 3 presents our analyses of the similarities and differences between the MISR retrievals and the aircraft observations, as well as a set of proposed aerosol aging mechanisms that act to change the particle properties downwind. Conclusions and plans for future work are given in Section 4.

2. Materials and Methods

The controlling factors behind fire emissions, such as burning intensity and fuel type, can change both frequently and dramatically for a given fire, rendering useless for validation any inter-comparisons made between observations with significant time lags. This study therefore leverages the only near-coincident set of MISR and in situ observations from the FIREX-AQ campaign: the 06 August 2019 flight through the Williams Flats Fire plume in central Washington state. The NASA DC-8 aircraft conducted a "remote sensing" overpass within several minutes of the MISR overpass, and then observed the plume for a full hour of sampling approximately 2 h subsequently. During the time between observations, plume geometry changed noticeably, most likely as a result of wind-driven advection (Figure 1). However, as shown later, plume particle properties correlate reasonably well between the two sets of observations for smoke of similar age.

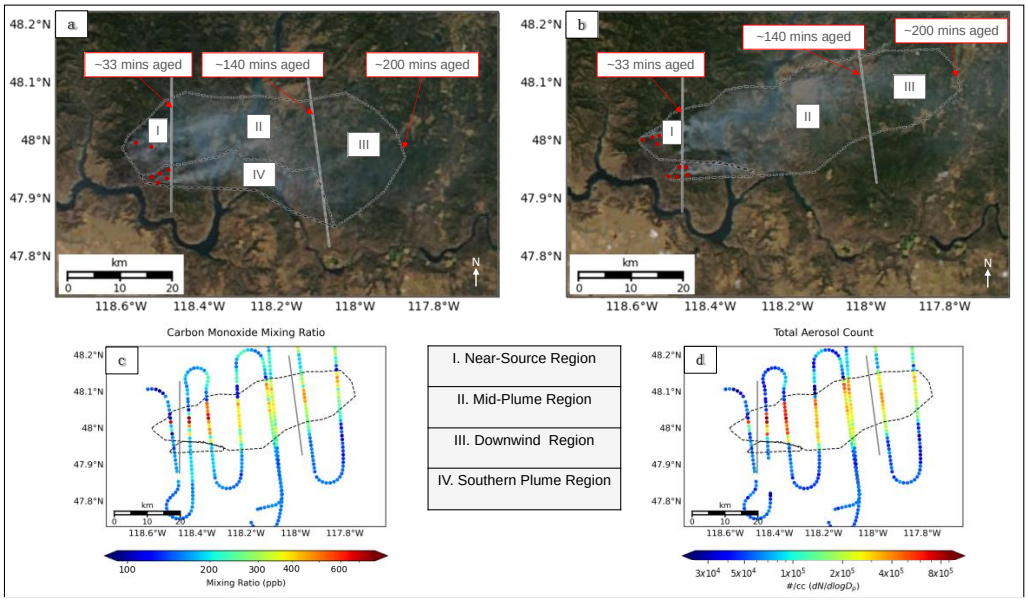

Figure 1. The Williams Flats Fire as seen on 06 August 2019: (**a**) at Multi-Angle Imaging Spectrometer (MISR) overpass time (19:06 UTC; MODIS Terra RGB image), and (**b**) during the Fire Influence on Regional to Global Environments Experiment-Air Quality (FIREX-AQ) flight operations (20:50 UTC; MODIS Aqua RGB image). The red dots indicate MODIS-identified hot spots, used to estimate source location. The dashed lines represent plume outlines we use for analysis. At both observation times, the plume is divided into distinct regions (I-III) based on estimated plume age, to allow for easy, qualitative comparison of inter- and intra-plume properties. At the time of MISR observation, there is an additional region (IV) that separates the southern-most plume from the other regions. The differential absorption CO measurements instrument (DACOM) CO mixing ratio and the laser aerosol spectrometer (LAS) total aerosol concentration observed by the aircraft (above 0.09 μm in diameter) are displayed in (**c**) and (**d**), respectively.

Several obstacles to comparing satellite and in situ observations determine how a validation study such as this must proceed [35]. These include (but are not limited to): (1) differences in temporal and spatial sampling; (2) varying instrument uncertainties and assumptions in the satellite retrieval algorithms; and (3) differences between column-integrated quantities measured by passive satellite sensors and direct measurements at specific 3d locations obtained from aircraft. These challenges must be taken into consideration when comparing results from the two sources. For example, the FIREX-AQ aircraft instruments might find locally extreme values, even if they observe only a small fraction of the BB smoke, whereas MISR averages the signal horizontally over ~1.1 km or more, and vertically over the entire column. Conversely, MISR observes a larger portion of the smoke overall, and may find different signals in parts of the plume not sampled by the aircraft. For the current study, we face the additional challenge of a 1–3 h time difference between the satellite and in situ observations. We address these issues by: (1) focusing the satellite-aircraft comparison on the general *trends* in particle properties along the length of the plume rather than the absolute values of those properties at specific locations; (2) where possible, using estimated plume-age horizons at the time of the respective measurements as the basis for comparison; and (3) taking into account the differences in spatial and temporal sampling between the observations when assessing the reported differences in aerosol properties.

2.1. MISR

The MISR instrument is in a polar orbit and has a swath width of ~380 km. As such, it samples locations at the equator approximately once every nine days, and every two days near the poles; over much of the planet, coverage occurs about once per week on average. MISR offers unique, multi-angle imagery [36] that makes it possible to retrieve height and motion vectors for clouds and aerosol plumes. This geometrical approach to retrieving plume height relies on the parallax of contrast features within the plume; therefore, plume features must exhibit sufficient optical thickness and contrast, relative to the surface, to derive plume height with this method. The MISR Interactive Explorer (MINX) software tool [37,38] nicely accomplishes these retrievals and was used to derive stereo heights and associated wind vectors for the plume in this study. With MINX, the user manually defines the plume source, plume extent, and wind direction in the MINX imagery to retrieve heights and winds locally. MINX has been used in a number of studies, including but not limited to retrieving heights and winds for volcano, wildfire, and dust plumes [35,39–50]. Under good conditions, MINX plume height estimates are accurate within +/−0.5 km or better. Retrieved plume height and wind vectors help determine smoke source and age as well as whether the plume was injected above the PBL. In this study, we use the retrieved wind vectors and distance from the source to approximate smoke age at various points throughout the plume, such that the comparison with the aircraft data can be focused on relating elements of similar age.

The MISR research aerosol algorithm (RA) [51,52] was used to retrieve aerosol optical depth (AOD), particle extinction Ångström exponent (ANG; calculated from measurements at 446 and 866 nm), particle single scattering albedo (SSA) and its spectral dependence, and particle shape, all indicative of "aerosol type." The intended use of the RA (e.g., for pollution studies, or for wildfire, volcano, or dust plumes) determines the specific set of aerosol components, each having different microphysical properties, to be included in the algorithm climatology. The particle property information content of MISR observations is qualitative, amounting to three to five size bins (e.g., "small," "medium," and "large"), two to four bins in SSA, and spherical vs. randomly oriented non-spherical particle shapes, under good retrieval conditions [53,54]. For this study, the RA includes one non-spherical component (a soil or dust grain optical analogue, based on an optical model derived in [55]) and 16 spherical components ranging in size and SSA values (Table S1 in the Supplementary Materials). For light-absorbing aerosols, particle type is further classified based on the spectral variation in absorption across the visible and near infrared spectrum, where "flat" aerosols display little to no wavelength dependence and are representative of typical urban pollution or BC particles, whereas "steep" aerosols exhibit greater absorption at shorter wavelengths and are more similar to

BrC from wildfire smoke [10,19,51,56]. This particle climatology is identical to the one used in Paper 1. For each 1.1 km MISR pixel, the RA calculates AOD values for each particle component to create a best-guess mixture of the aerosol plume composition, such that the simulated top-of-atmosphere (TOA) reflectances best match those observed in the MISR multi-angle, multi-spectral measurements. This method has already been used for global aerosol typing [48] and for characterizing particle type in volcanic and wildfire plumes [29,43,46–48].

The particle property information derived from the MISR satellite data is based on column-effective, optical measurements rather than from direct sampling. In both the current and previous work, we therefore refer to the RA measurements of particle size and light absorption as the *retrieved effective particle size* (REPS; μm) and the *retrieved effective particle absorption* (REPA; dimensionless), respectively. These terms help reflect both the measured content and the limitations of the retrieved quantities. Particle property information is reduced when the mid-visible AOD is below about 0.15 or 0.2, but this is not a concern for well-defined smoke plumes. Along-plume changes in AOD, REPS, and REPA combined with available meteorological data and MINX stereo heights can help constrain the relevant aging mechanisms for a plume observed under good retrieval conditions. For example, decreasing AOD accompanied by decreasing REPS downwind may indicate size-selective gravitational settling, whereas uniform particle deposition would feature decreasing AOD accompanied by relatively constant REPS. Similarly, constant AOD accompanied by increasing REPS downwind might indicate particle aggregation, whereas constant or increasing AOD accompanied by decreasing REPS may suggest the formation of secondary aerosols. These and other patterns have been observed with MISR in volcanic plumes (e.g., [47,48]).

The operation of the RA is described by Limbacher and Kahn [51,52]. Several recent advancements to the RA that increase particle property sensitivity are described in Paper 1. Details on the 17-component optical and physical properties included in the RA climatology are given in Table S1 in the Supplementary Materials.

2.2. Aircraft Data

The FIREX-AQ campaign was conducted to investigate the impact of wildfire and biomass burning smoke on air quality and weather, with particular emphases on relating trace gas and aerosol emissions to fuel type and fire conditions at the point of emission, understanding downwind chemical transformation of smoke, and assessing the efficacy of satellite detections for estimating emissions [57]. From 22 July to 19 August 2019, the NASA Douglas DC-8 research aircraft flew through wildfire plumes in the vicinity of Boise, Idaho, before moving to Salina, Kansas for the remainder of August and the first week of September to study agricultural burns in the southeast U.S. Among the many instruments with which the DC-8 was equipped, we focused mostly on measurements of aerosol size distribution, SSA, and particle shape to which MISR is sensitive. We included basic meteorology and gas chemistry measurements as needed. We also introduce the use of airborne lidar data, which was not available for our previous validation study in Paper 1. Most in situ measurements are acquired at sufficiently high temporal resolution (0.2–10 s, depending on instrument) that at DC-8 cruising velocity (~200 m/s) they had to be aggregated for comparison with the 1.1 km MISR retrieval regions. Instrument noise smoothing was also required. We therefore parsed the aircraft data into ~1.1 km bins and obtained the median measurement values, acquisition times, and locations for further analysis.

2.2.1. Aerosol Optical Properties

The degree of light absorption by BB aerosols is a critical indicator of particle type and aging. We derive particle SSA from aerosol absorption, measured by the particle soot photometer (PSAP), and scattering from the nephelometer, both acquired at 1 s intervals ([58]: PSAP/neph). The nephelometer measures total as well as hemispheric aerosol scattering at 450, 550, and 700 nm by detecting the aerosol-scattered light and subtracting that scattered by the air. The nephelometer data provided were corrected using methods described by Anderson and Ogren [59]. The PSAP

measures absorption continuously at three visible wavelengths by monitoring changes in transmittance through a filter, using a three-wavelength light-emitting diode (LED) (470 532, and 660 nm). As the filter transmittance can also change from the deposition of scattering aerosols, correction methods using scattering measurements from the nephelometer, based on those described by Virkkula [60], were applied by the field scientists. The uncertainty of both the PSAP and nephelometer measurements are estimated at 5%. At some points, in cleaner atmospheres where the nephelometer signal approached its detection limit, small negative scattering and absorption coefficients were reported. Therefore, SSA was only calculated in cases where scattering coefficients were >-3 Mm^{-1} and absorption coefficients were >-5 Mm^{-1}.

To help identify BrC, which is more absorbing in the UV than the mid-visible range, we analyzed aerosol absorption measurements at 405 and 664 nm made by the photoacoustic soot spectrometer (PAS) ([58]: PAS). The PAS measures aerosol light-absorption directly by detecting acoustic waves generated by the absorption and subsequent heating of particles exposed to modulated laser light. The hallmark of this technique is that it is insensitive to aerosol light scattering; this is incredibly valuable, as scattering is usually the chief aerosol light-extinction mechanism. The accuracy of the dry measurement varies but is considered within +/−20%.

Aircraft lidar measurements were obtained from the dual NASA Langley differential absorption lidar (DIAL) and high spectral resolution (HSRL) system (or DIAL-HSRL) ([58]: DIAL-HSRL). The DIAL-HSRL instrument uses five lasers to acquire ozone vertical profiles simultaneously with aerosol backscatter profiles in the visible (532 nm) and near-infrared (1064 nm). The DIAL-HSRL also measures aerosol extinction at 532 nm and depolarization at 532 nm and 1064 nm. The HSRL technique separates the aerosol and molecular signals, so aerosol extinction and backscatter are measured independently [61]. Retrieved intensive aerosol properties have been used to classify aerosol mixtures. Specifically, aerosol depolarization at each wavelength provides an indication of particle non-sphericity, the extinction/backscatter ratio (i.e., the lidar ratio) at 532 nm offers a loose constraint on particle composition, and the 1064 nm/532 nm color ratio is related to particle size [62–65]. During the FIREX flight on 06 August 2019, the DC-8 performed three "remote sensing" longitudinal passes above the plume along its length, during which the DIAL-HSRL made soundings. In addition, lidar data were acquired for the eight across-plume transects within the plume, as the DC-8 in situ instruments also sampled the smoke plume. The first longitudinal overpass (referred to here as L1) occurred at approximately 19:00 UTC and is most nearly coincident with the 19:07 UTC MISR overpass; L2 took place ~20:30 UTC and L3 at ~21:50 UTC. The across-plume transects were flown between L2 and L3. For the locations of all the transects within the plume, see Figure S3 in the Supplementary Materials.

2.2.2. Aerosol Microphysical Properties

Biomass burning is a major global source of accumulation-mode aerosols ($D_p < 1$ μm) in the atmosphere, and the vast majority of BB particulate emissions are within this size range [13,14]. However, wildfires can also inject soil or dust particles into the air near the source with $D_p > 1.0$, and even small changes in the size distribution for accumulation-mode particles can provide clues about particle type, age, and formation as well as atmospheric chemistry and burning conditions. We utilize 1 s measurements of aerosol size and number concentration from the TSI-3340 laser aerosol spectrometer (LAS) ([58]: LAS), which measures the light scattered by particles that pass through a He-Ne laser beam, to determine particle size. The instrument sizing was field-calibrated using size-classified ammonium sulfate aerosols (refractive index of 1.52 + 0i) The LAS uses wide-angle optics to capture particle sizes across a large diameter spectrum (with an estimated uncertainty of ~20% in this case), although for the purpose of this study, we only leverage data for particles within the approximate size range to which MISR is sensitive (~0.05 to 3.5 μm in diameter). In order to more directly compare aircraft size distributions with those observed by MISR, we summed the concentrations of multiple LAS size bins into larger size categories such that the mid-point effective radius (r_e) of the category approximates that defined by the RA climatology (Table S1 in the Supplementary Materials), as follows:

- "Very small aerosols"—Particles with D_p ranging from ~0.09 to ~0.18 μm.
- "Small aerosols"—Particles with D_p ranging from ~0.18 to ~0.3 μm.
- "Medium Aerosols"—Particles with D_p ranging from ~0.3 to 0.9 μm.
- "Large Aerosols"—Particles with D_p ranging from ~0.9 to 3.45 μm.

It should be noted that the size categories here are compared against the *qualitative* size categories retrieved by MISR, and so small discrepancies in bin definitions represent inherent uncertainty in our analysis. We also illustrate size via the transect-mean particle size distributions and estimate changes in the width of the distribution with approximations of $D_{(10\%)}$, $D_{(50\%)}$, and $D_{(90\%)}$, representing the sizes below which 10%, 50%, and 90%, respectively, of the total aerosol populations exist (within the range of observed sizes). $D_{(50\%)}$ is typically considered to represent the "mean" aerosol size.

The hygroscopicity of BB aerosols might serve as a qualitative indicator of mixing state and age, particularly as it pertains to the evolution of BC. Although pure, freshly emitted BC is hydrophobic, these particles can become increasingly hydrophilic and may serve as CCN with increased age due to a combination of coagulation with more water-soluble species and condensation of volatile gases onto the particle surface [14,66]. To determine which aerosols could serve as CCN in the Williams Flats plume, we considered measurements at 1 s intervals from a DMT cloud condensation nuclei counter 100 (CCN-100) ([58]: CCN), which applies a thermal gradient across a continuous-flow diffusion chamber to create a supersaturated environment where water vapor can condense onto particles. Particles that grow to at least 0.75 μm are considered activated and are then sized by the optical particle counter. For FIREX, the chamber was maintained at 0.34% supersaturation (with 0.04% supersaturation uncertainty), meaning particles that are counted as CCN here are those that activate at 0.34% supersaturation or higher. The supersaturation was calibrated using ammonium sulfate aerosols following Rose et al. [67] and Moore et al. [68]. The concentrations given by the CCN-100 have a reported 10% uncertainty.

2.2.3. Air and Particle Chemistry

To account for plume dilution, in some parts of our analysis, we applied 1 s carbon monoxide (CO) measurements from the differential absorption CO measurement (DACOM) instrument [69,70], that operated with ~2% uncertainty for the sampling period over Williams Flats ([58]: DACOM). Along with several other trace gases, CO is a frequently used tracer for plume dilution via the derived normalized excess mixing ratio (NEMR), defined as the ratio of the excess species of interest (ΔX) to the background-corrected CO (ΔCO). The NEMR has been used in previous studies to help identify secondary formation of organic aerosol (OA) and inorganic aerosols in smoke plumes with measurements of particulate matter and OA mass [21].

The oxidation of aerosols occurs naturally as they interact with background air, altering the properties of organic aerosol components and usually increasing SSA and hygroscopicity. The degree of atmospheric processing of the smoke plume was estimated using an independent proxy measurement for oxidation, defined here as $-1\log_{10}(NO_x/NO_y)$, where NO_x is the steady-state mixture of NO and NO_2, and NO_y is the sum of NO_x and the products formed when NO_x is oxidized (i.e., HNO_3, peroxyacetyl nitrate (PAN), and organic nitrates). For this, we used nitrogen oxide measurements collected with an ozone-induced chemiluminescence technique reported at +/− 5% uncertainty ([58]: Nitrogen oxides). As NO_y is nearly conserved on timescales of less than one day, changes in the NO_x/NO_y ratio likely represent oxidative processes. Although not a quantitative measure of oxidation, this method has been shown to correlate well with O/C ratios, that are commonly used to measure photochemical oxidation and SOA formation [71,72].

As BC is the most important climate influencer in smoke plumes, direct measurements of BC mass are very valuable. Refractory black carbon (rBC) mass measurements from the single-particle soot photometer (SP2) were analyzed to help characterize particle type and mixing state ([58]: SP2). The SP2 derives mass concentrations of rBC by measuring the amplitude of incandescence signals produced as rBC-containing particles traverse a continuous-wave laser beam, offering a ~20% level of

uncertainty in this case. The detection size range for rBC particles is 0.09–0.55 μm in diameter. For the remainder of this paper, we refer to rBC using the more qualitative label "BC", as this is how we would identify refractory black carbon particles in satellite retrievals.

2.2.4. Burning Characteristics, Smoke Age, and Fuel Type

The progression of smoke aging is nonuniform within a plume due in part to variability in wind direction and speed, both of which also affect changes in plume geometry between non-coincident observations. Therefore, as with the satellite data, we determine smoke age at various points throughout the plume based on wind speed and distance from the source. For the aircraft observations, this is based on wind speeds measured by the on-board meteorological measurement system (MMS). Ages were calculated by one of the FIREX managers ([58]: Fire Flags), using a vertical profile of wind speed averaged from measurements on the DC-8 acquired within 2 degrees of the fire latitude/longitude. A single horizontal-transport time was estimated from the mid-point altitude, latitude, and longitude for each perpendicular transect of each smoke plume, assuming straight-line horizontal advection from the fire to this aircraft position.

As has been mentioned, smoke particle properties are largely dependent on fuel characteristics and burning regime, with smoldering conditions being more prevalent in fuels consisting of large woody debris such as branches and dead fallen trees, whereas flaming conditions are associated more strongly with fine fuels such as grasses, shrubs, and small deadwood [73,74]. We use fuel type reports from the incident information system [75], land cover type from the MODIS satellite instrument (MCDQ1, Collection 6), and modeling from the fuel characteristic classification system (FCCS) ([58]: Fuel2Fire) to link the observed particle properties from MISR with fire burning characteristics. We also attempt a more quantitative approach to determining burning conditions via the modified combustion efficiency (MCE; Equation (1), where ΔCO_2 and ΔCO represent the difference between the species' concentrations inside the plume vs. background levels outside the plume). As flaming combustion is more efficient than smoldering combustion and produces more CO_2 relative to CO [73], MCE values for flaming combustion are expected to be large, typically above 0.9, whereas MCE values for smoldering combustion are lower and vary over a range of ~0.65–0.85 [22]. The changes in MCE between transects help shed light on the degree to which the observed changes in particle properties are a function of burning conditions at the source, as distinct from subsequent atmospheric processing; this was not possible with the data available for Paper 1. We use transect-averaged MCE values calculated and provided by a FIREX Manager ([58]: Fire Flags), where CO and CO_2 mixing ratios were those measured by the DACOM and LI-COR 7000 ([58]: LI-COR) instruments, respectively. The LI-COR instrument measures CO_2 via non-dispersive infrared spectroscopy with a reported accuracy and precision of 0.25 and 0.1 ppm, respectively [76].

$$MCE = \frac{\Delta CO_2}{\Delta CO_2 + \Delta CO}. \quad (1)$$

3. Results and Discussion

The Williams Flats Fire ignited on 02 August due to lightning from a band of early morning thunderstorms, burning primarily in the Confederated Tribes of the Colville Reservation and Washington Department of Natural Resources protected lands. The bulk of the fire activity was confined to 02 through 09 August, at which point a large precipitation event stifled burning so that the fire was effectively extinguished in subsequent days. However, re-invigoration and creeping activity resulted in continued management efforts through 25 August, by which time over 44,000 acres had burned [75]. The fire was managed with both aviation and on-the-ground containment methods including helicopter water drops, air tanker retardant drops, building a direct line, and significant mop-up [75]. However, active fire suppression was not occurring during the FIREX-AQ operations on 06 August. The fuels involved were reportedly a mixture of timber, short grass, light slash from logging, and a coniferous overstory [75]; similarly, the MODIS Level 3 IGBP yearly land cover type shows

the region is a mixture of grassland, savanna, and evergreen needleleaf forest, and fuel characteristic classification system (FCCS) modeling reveals primarily Douglas-fir-Pacific ponderosa pine was burning, followed by wheatgrass grassland ([58]: Fuel2Fire).

The plume produced by this fire was observed by MISR on 06 August 2019, at ~19:07 Universal Coordinated Time (UTC), ~2 h before the FIREX DC-8 aircraft sampled the same area (for all but a first "remote sensing" overpass at ~19:00 UTC); the aircraft continued sampling this plume for an additional hour. During all observation times, it is clear the fire contained two main hotspots: a northern one that produced a large plume, and another to the south and east that produced a smaller plume burning slightly uphill (Figure 1). At the time of MISR observation, the distinction between these plumes is clear and the smoke displays unique patterns in optical and physical properties that can be linked to smoke age. We divide the MISR-observed plume into four regions based on these patterns: a near-source region (designated Region I), a mid-plume region (II), a downwind region (III), and a southern plume region (IV) (Figure 1a). It should be noted that despite the clear distinction between the northern and southern plumes, there is still likely some degree of mixing, especially downwind. There is also optically thin smoke outside the plume boundaries both downwind to the east as well as to the north in the river valley. We exclude these from our analysis because very thin smoke layers cannot be retrieved reliably by MINX or the RA, so the focus of this study is on relatively thick smoke within the plume. We calculate the approximate age of the smoke at regional boundaries using the ratio of the along-plume distance and mean wind vectors in the area derived from MINX (Figure S1 in the Supplementary Material). Estimated plume ages at the regional transition lines are given in Figure 1. It should be noted that these dividing lines only apply to the northern plume. The southern plume is treated as its own distinct region (Region IV) as its particle properties are fairly uniform at the level of detail we can retrieve from the satellite; and so its age is averaged across its entire length. The mean MINX-derived wind speeds in Region IV are greater than in the northern plume area (4.26 ± 1.66 vs. 3.88 ± 1.96 m/s; Figure S1 in the Supplementary Materials) and the source is located further east, so smoke here is approximately 20 min younger than smoke at a similar downwind distance in the northern plume.

By the time the aircraft began its sampling two hours later, the northern and southern plumes had largely merged and only a small area of smoke near the south-east hotspot was clearly distinct from the rest (outline in Figure 1b). Due to altitude limitations, the aircraft did not sample this area in Transect 1, whereas subsequent transects sampled smoke from the merged northern and southern plumes where smoke had converged. We therefore do not define a Region IV for the FIREX plume, and, as shown subsequently, downwind particle properties from the aircraft do not display the same north-south differences seen by MISR. Based on plume ages derived from the aircraft wind speeds, the rest of the plume was divided into regions of similar age as the MISR-observed northern plume (Figure 1b). However, because Region I contains only points sampled from the northern plume (Transect 1) and Region II experiences an influx of fresh smoke from the southeast source (Transects 2 and 3), the broad regional averages for many measurements are skewed and do not fully illustrate the along-plume changes in particle properties. We therefore focus the analysis of the in situ measurements on transect-by-transect changes, and return to regional analysis in later discussion.

In this section, we compare the particle properties retrieved by MISR with those obtained in situ from aircraft measurements, paying particular attention to changes with downwind distance. We then apply this information to current knowledge on how various aging mechanisms impact particle properties, in an effort to infer the active processes at hand. Only observations taken within the plume boundaries (Figure 1) are included in our analysis, except when comparing measurements to background values. For the MISR dataset, the boundary is a user-drawn plume outline created during the MINX retrieval (Figure 1a). For the FIREX dataset, the RGB MODIS-Aqua image, acquired minutes before FIREX sampling began, was used to draw the plume outline (Figure 1b), with slight adjustments based on aircraft-derived aerosol and CO concentrations that reflect potential changes in plume geometry over the duration of the flight after the MODIS image was captured (Figure 1c,d). Where applicable,

all figures display the plume boundary as a dotted-line polygon and the dividing lines between regions are shown as thin solid grey lines.

3.1. Satellite Observations

We first provide an overview of the satellite observations, with emphasis on the differences in smoke particle properties between regions. Figures 2 and 3 respectively contain the MISR-MINX stereo heights and wind vectors and the standard MISR RA latitude/longitude plots of AOD, SSA_{558}, and $ANG_{446\text{-}866}$. In addition to these, we map, in terms of both retrieved absolute AOD and AOD fractional component: the spectral dependence of aerosol light absorption via the separate sums of retrieved (1) spectrally flat (BC analog) and (2) spectrally steep (BrC analog) aerosol components (Figure 4a–d), (3) the retrieved aerosol shape via the non-spherical component (Figure 4e,f), (4) further information on light-absorption via the sum of all non-absorbing components (Figure 4g,h), and (5) further information on aerosol size via the separate sums of very small, small, medium, and large aerosols (Figure 5). (See Table S1 in the Supplementary Materials for the precise size and absorption properties of these components). Plots of absolute AOD map the AOD that can be attributed to the specific component(s) retrieved, whereas fractional AOD plots highlight the dominant characteristics of the plume over its extent. As discussed subsequently, these particle properties are, for the most part, neatly distinctive between the four plume regions. It is important to reiterate that, when considering specific particle types (e.g., black carbon, brown carbon, soil/dust, non-absorbing aerosols), the MISR-retrieved aerosol properties represent the optical equivalent of the true smoke particle mixture, which is not necessarily a mixture of the specific components retrieved from among those prescribed by the RA climatology [35,47,48,54]. Note that the missing retrievals in the RA results are pixels located above the river, as the version of the RA used in this study is geared for land observations only (future versions will include an over-water component). Table 1 quantifies the above-mentioned RA observations, providing the mean, standard deviation, and median satellite-retrieved particle properties for each region. A more detailed discussion of these statistics can be found in the Supplementary Materials.

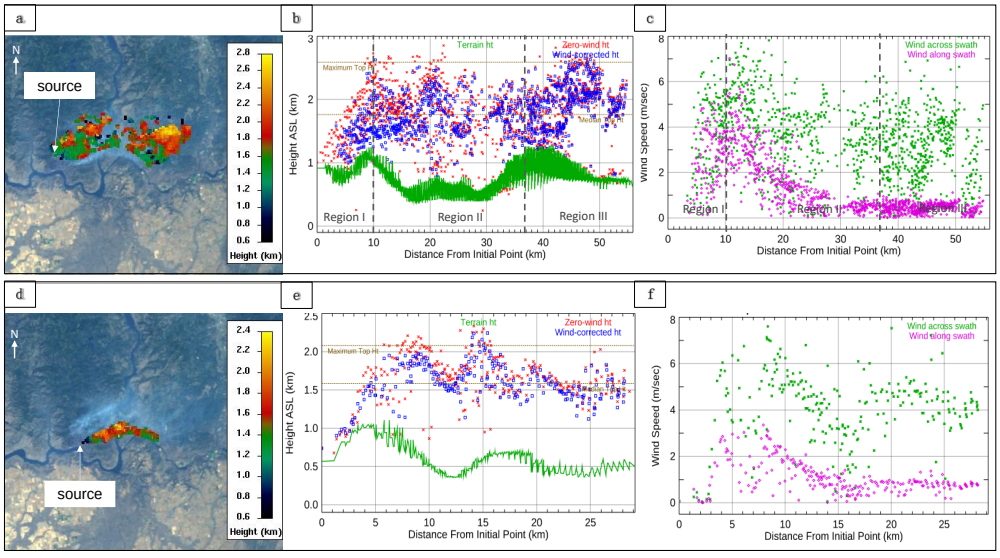

Figure 2. Height and wind properties for the Williams Flats Fire retrieved by MISR at 19:06 UTC (Orbit 104434, Path 45, Block 52) on 06 August 2019. The top panels (**a**–**c**) correspond to retrievals for the northern plume, whereas the bottom panels (**d**–**f**) correspond to the southern plume. Panels (**a**,**d**) are MISR-MINX stereo height retrieval map; (**b**,**e**) are MINX stereo height profiles as a function of distance from the source, for both zero-wind (red) and wind-corrected (blue) analyses, with surface elevation indicated in green; and (**c**,**f**) are the across-swath and along-swath wind vectors. The dashed grey lines in panels (**b**) and (**c**) represent the dividing lines between regions in the northern plume defined in Figure 1.

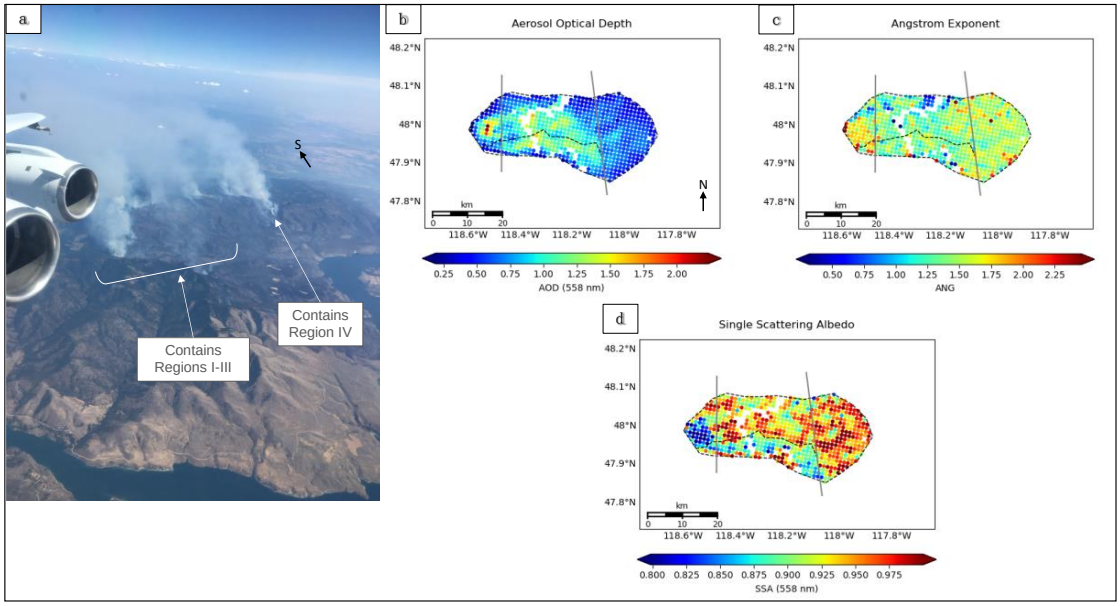

Figure 3. Basic plume properties for the Williams Flats Fire retrieved with the MISR RA at 19:06 UTC (Orbit 104434, Path 45, Block 52) on 06 August 2019, accompanied by a contemporaneous image of the fire (**a**) taken from the aircraft during sampling [credit: K. Junghenn Noyes]. This image highlights the distinction between plume regions (labeled). MISR RA results are given in panels (**b**) AOD at 558 nm; (**c**) 446–866 nm extinction Ångström exponent (ANG); and (**d**) single scattering albedo (SSA) at 558 nm. The transects for estimated plume ages corresponding to the region boundaries in Figure 1 are indicated with thin grey lines.

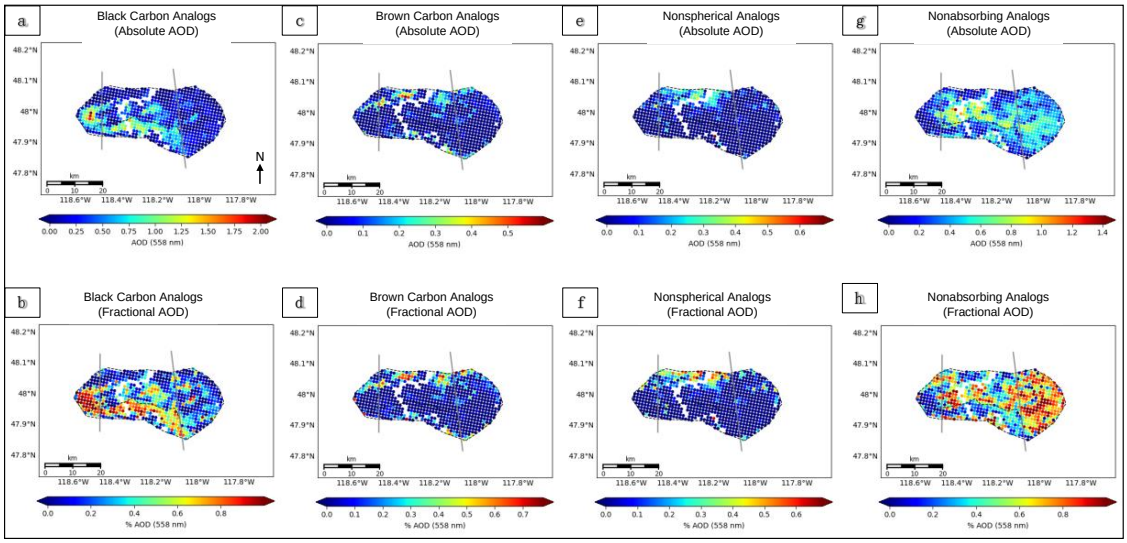

Figure 4. The absolute and fractional AOD (558 nm) of various MISR-RA aerosol components for the Williams Flats Fire on 06 August, 2019, where (**a**,**b**) are the sum of all spectrally "flat" or BC-like components, (**c**,**d**) are the sum of all spectrally "steep" or BrC-like components, (**e**,**f**) are the sum of all non-light-absorbing components, and (**g**,**h**) are the non-spherical, dust-like components. Fractional plots are given as a fraction of 1. Note: scales differ between panels.

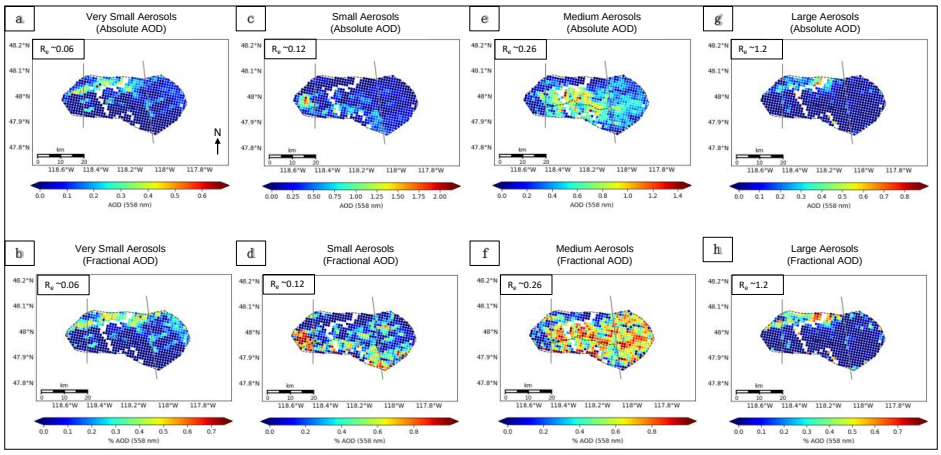

Figure 5. The absolute and fractional AOD (558 nm) of various MISR-RA aerosol size bins for the Williams Flats Fire on 06 August, 2019, where (**a**,**b**) are the sum of all "very small" components, (**c**,**d**) are the sum of all "small" components, (**e**,**f**) are the sum of all "medium" components, and (**g**,**h**) are the sum of all "large" components (which includes the non-spherical analog). Particles are assumed to be normally distributed around the effective radius (R_e) provided in the legend. Note that "large" aerosols (**g**,**h**), include both the large spherical nonabsorbing component (R_e = 1.28) and the non-spherical component (R_e = 1.21). Fractional plots are given as a fraction of 1. Note: scales differ between panels.

Table 1. MISR-observed particle properties for the Williams Flats fire by region. AOD—aerosol optical depth; SSA—single scattering albedo (558 nm); ANG—extinction Ångström exponent (446–866 nm).

Plume Region:		**Near-Source (Region I)**	**Mid-Plume (Region II)**	**Downwind (Region III)**	**Southern (Region IV)**
AOD	Mean	0.8750	0.8653	0.5965	0.9196
	±σ	±0.4550	±0.2565	±0.1123	±0.2840
	Median	0.8499	0.8747	0.6002	0.9500
SSA	Mean	0.8773	0.9402	0.9549	0.9034
	±σ	±0.06045	±0.03135	±0.03325	±0.04425
	Median	0.8659	0.9411	0.9574	0.8979
ANG	Mean	1.568	1.325	1.5206	1.424
	±σ	±0.3450	±0.2831	±0.1887	±0.2857
	Median	1.620	1.349	1.504	1.418
BC [a,b]	Mean	0.6026	0.2559	0.2170	0.5623
	±σ	±0.3797	±0.2349	±0.2204	±0.2993
	Median	0.7459	0.1995	0.1591	0.6305
BrC [a,c]	Mean	0.08076	0.1130	0.06004	0.06354
	±σ	±0.1471	±0.1825	±0.1236	±0.1337
	Median	0	0.004544	0	0
Non-absorbing [a,d]	Mean	0.2657	0.5022	0.6870	0.3610
	±σ	±0.2787	±0.2691	±0.2559	±0.2703
	Median	0.1782	0.4733	0.7416	0.3020
Non-spherical [a,e]	Mean	0.05080	0.1286	0.03584	0.01307
	±σ	±0.1139	±0.1745	±0.08294	±0.06604
	Median	0	0.03690	0	0

[a] In terms of fraction of total AOD (0 to 1); [b] The combined total of all spectrally flat components, which is meant to represent black carbon; [c] The combined total of all spectrally steep components, which is meat to represent brown carbon; [d] The combined total of all non-absorbing components; [e] The only non-spherical component, meant to represent dust or soil.

The MISR–MINX stereo heights indicate that both the northern and southern plumes are concentrated mostly within 2 km above sea level (ASL) at 19:07 UTC, with median and maximum heights of 1.76 and 2.59 km (northern) and 1.59 and 2.08 km (southern), respectively (Figure 2b,e). The RA-retrieved particle properties indicate peak mid-visible AOD of up to ~2.2 near the source,

systematically decreasing with downwind distance to a minimum of <0.2 in some pixels of Region III, within the area we defined as the observable plume in the satellite imagery (Figure 3b). Both plumes are overall comprised of fine particles (ANG > 1), although there is a small area of larger particles in the northern plume along its northern edge, particularly in Region II. REPS is particularly low near the northwest source (Region I), increases in Region II, and subsequently decreases again in Region III (Figure 3c, Figure 5). Component analysis suggests the increased REPS in Region II is driven by both absolute and fractional increases in medium- and large-sized particles, accompanied by a decreased contribution from small-sized particles, whereas the decreased REPS in Region III is driven by absolute and fractional decreases in large-sized particles alone (Figure 5). REPS in the southern plume is relatively constant throughout the plume length and is overall somewhere between the values seen in Regions I and II of the northern plume. As seen in Figure 5, particle size here is almost exclusively a mixture of small and medium particles, as compared to the combination of all four size categories seen in the northern plume (although small and medium categories still dominate in the northern plume).

The northern plume REPA spans the entire range of possible SSA values as defined in the MISR RA climatology, with significant absorption near the source in Region I (SSA~0.8) that gradually decreases downwind to the point where the majority of pixels in Region III exhibit SSA >0.95 (and some as high as 1.0) (Figure 3d, Table 1). REPA is somewhat variable throughout Region II, with distinct alternating patches of less absorbing aerosols (SSA >0.95) and more absorbing aerosols (0.90 < SSA < 0.95). Conversely, the southern plume REPA is more consistent, with most SSA values below 0.90 throughout the length of the plume, in-between the average values seen in Regions I and II of the northern plume. Component analysis suggests that smoke from the northwest source (Region I) is largely a BC-dominated mixture, but that subsequent regions of the northern plume increasingly transition to mixtures interpreted as mostly non-absorbing and BC particles. However, a significant portion along the northern edge of Region II is retrieved almost entirely as a mixture of BrC and non-spherical analogs. This is the same area of the plume where sizes are retrieved as a combination of very small and large particles, suggesting that smoke here might contain a mixture of very fine organic and large soil- or dust-like aerosols. In the southern plume, the mixture is almost entirely BC and non-absorbing particles, with the former being dominant overall and decreasing only slightly with downwind distance (Figure 4, Table 1). Note that the MISR-retrieved component AOD values and fractions represent an interpretation of the MISR column-integrated reflectances in terms of the components included in the RA (Table S1 in the Supplementary Materials), whereas the REPS and REPA are less dependent on algorithm assumptions. This is one reason why validation with the in situ data is so important.

Based on the satellite observations alone, we identify several processes that could be affecting plume particle properties. In particular, we infer that: (1) VOC condensation and/or coagulation of particles act to increase REPS in Region II compared to Region I; (2) gravitational settling leads to a preferential decrease in the fraction of large-sized particles in Region III compared to Region II; (3) there is an increase in the oxidation state of particles progressively downwind throughout the plume, reflected in the increased AOD of non-absorbing analogs; and (4) there may be differences in the emissions between the northern and southern hotspots, leading to observed differences in particle size and absorption. Mechanism (1) is supported by the *absolute* increase in medium-particle AOD at the expense of the absolute small- and very small-particle AOD, suggesting particles in smaller categories are transitioning to the larger size categories. This cannot be validated directly with available in situ measurements, but changes in the particle number concentration and particle size distribution as well as changes in the oxidation state can offer supporting indications. Mechanism (2) is supported by MISR-MINX plume heights, where the smoke column in the northwest plume approaches the surface approximately 40 km downwind at the beginning of Region III, so particles may be settling to the surface in this region (Figure 2b). As aircraft measurements sample a single elevation, this mechanism cannot be directly validated in situ. However, the differences between the satellite and aircraft size distributions can provide insight into how particles may be distributed within the atmospheric column

(e.g., [48]). Mechanism (3) can be validated from the available in situ data via the changing oxidation state, BC mass, and SSA downwind. Mechanism (4) may be supported by in situ data as well. We test these hypotheses with the FIREX data in subsequent sections.

3.2. In Situ Observations and Comparison with MISR

The satellite and in situ measurements are considerably similar in their characterization of particle property evolution as a function of smoke age, and most of the key differences in particle size and absorption can be attributed to differences in sampling and changes in the plume geometry between sampling times. Here, we assess the fidelity of the RA results by first presenting an overview of the aircraft observations and comparing them with the MISR-retrieved particle properties in the plume as a whole. We then provide detailed observations for along-plume changes in particle properties observed in situ, and assess how they connect to the MISR-observed properties. This step also allows us to demonstrate how the MISR-retrieved particle properties offer context for the aircraft data, providing critical information for understanding plume evolution and inferring particle aging mechanisms. These are summarized in Section 3.2.2.

As the distinction between the emitted smoke from the two main hotspots was no longer clear at the time of the FIREX aircraft observations, the in situ analysis focuses more on the differences in smoke properties between transects, rather than regions, although both are important to consider. We abbreviate across-plume transects using the letter T followed by the transect number (T1, T2, . . . , T8), and the longitudinal, nadir-viewing above-plume "remote sensing" transects with the letter L followed by the transect number (L1, L2, and L3). Figure 6 displays the lidar-retrieved aerosol backscatter (providing information on plume height and extent) and aerosol depolarization (providing information on particle non-sphericity) for L1-L3. Figures 7 and 8 illustrate, as latitude/longitude plots, the chemical, optical, and physical properties measured in the plume as described in Section 2.2. Each point represents the aggregated ~1.1 km median value of a given measurement. Figure 9 displays non-aggregated particle size distributions (in terms of both number and volume concentrations) by transect for points inside the plume outline, grouped into subplots based on the regions defined in Figure 1. Note that measurements for particles greater than 0.6 µm in diameter were not plotted, as their contributions to the measured aerosol abundance were negligible. Table 2 provides several non-aggregated, transect-averaged parameters from Figures 7–9 as well as transect age and MCE. This is supplemented by Table 3, which quantifies the regionally aggregated mean, standard deviation (SD or σ), and median values for many of the same measurements. As with the satellite observations, a comprehensive discussion of these statistics, plus the DIAL-HSRL measurements, can be found in the Supplementary Materials.

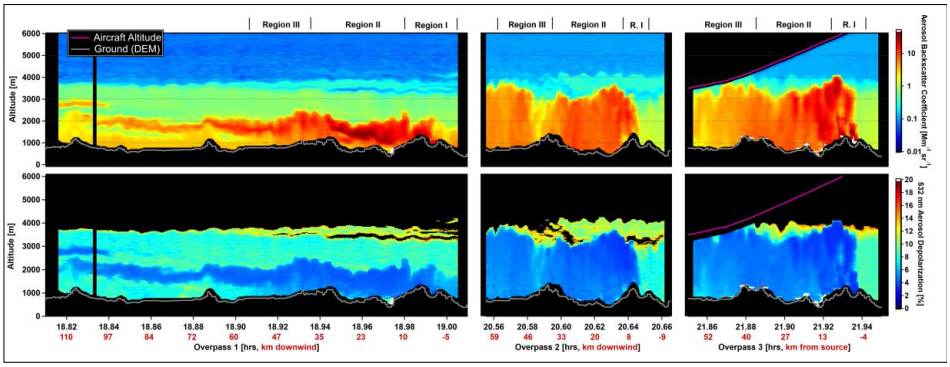

Figure 6. DIAL-HSRL nadir retrievals of 532 nm aerosol backscatter coefficient (**top row**) and depolarization ratio (**bottom row**) for the three longitudinal overpasses (L1-L3). During the MISR/MINX overpass (L1), the plume is less vertically developed and only reaches an altitude of approximately 2 km, consistent with the MISR/MINX retrievals shown in Figure 2. The anomalous high-scattering values very near the surface at ~[18.97, 20.66, and 21.88–21.92 h] are scattering contamination from the ground surface and should not be interpreted as aerosol signal. Note: Time is in UTC.

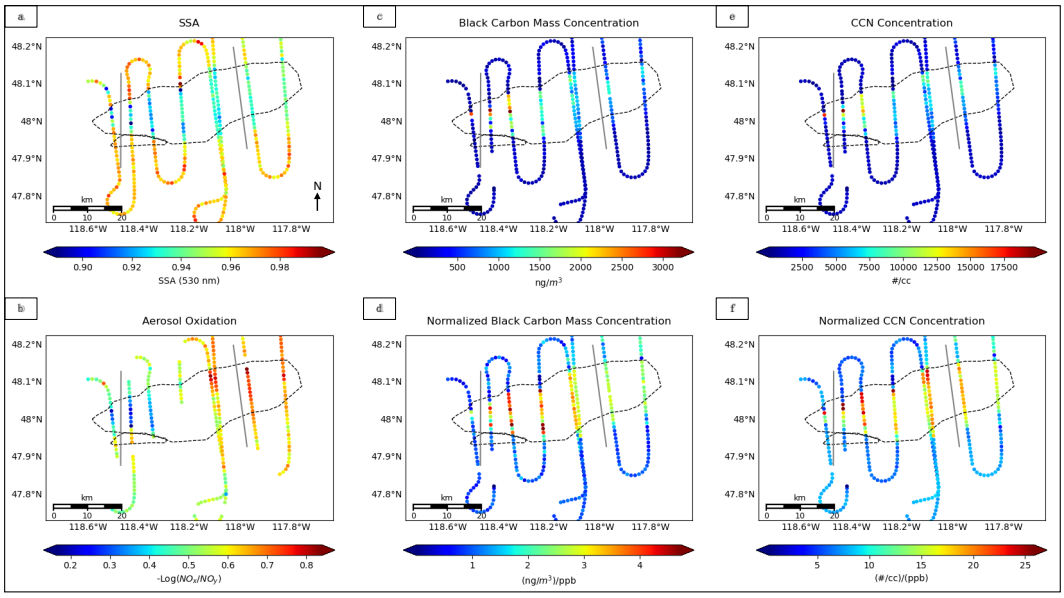

Figure 7. FIREX aircraft observations of the Williams Flats Fire on 06 August, 2019: (**a**) 530 nm SSA (PSAP/neph), (**b**) aerosol oxidation (derived from ozone-induced chemiluminescence), (**c**) Mass concentration of rBC (SP2), (**d**) rBC concentration normalized by CO (SP2, DACOM), (**e**) concentration of particles that can act as CCN at 0.34% supersaturation (CCN-100), and (**f**) CCN concentration normalized by CO (CCN-100, DACOM). The grey lines represent the boundaries between regions defined in Figure 1.

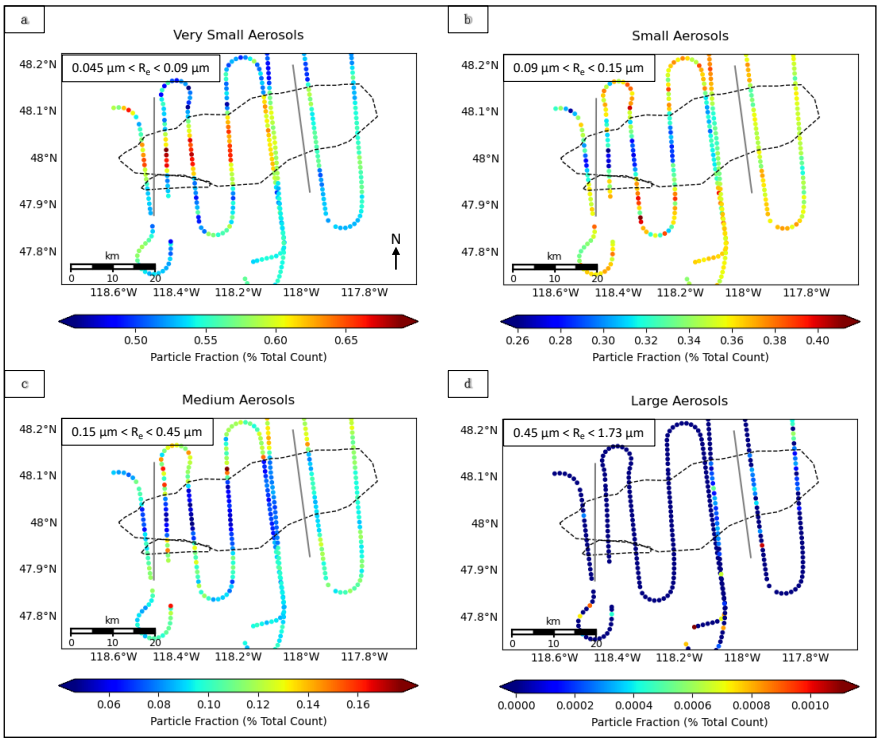

Figure 8. Fractional contributions (from zero to one) to the total aerosol count for very small (**a**), small (**b**), medium (**c**), and large (**d**) aerosols in the Williams Flats Fire, as measured by the LAS in situ instrument on 06 August 2019. The grey lines represent the boundaries between regions defined in Figure 1. Note: Approximate size ranges are given in the corner each plot, and the scales differ between categories.

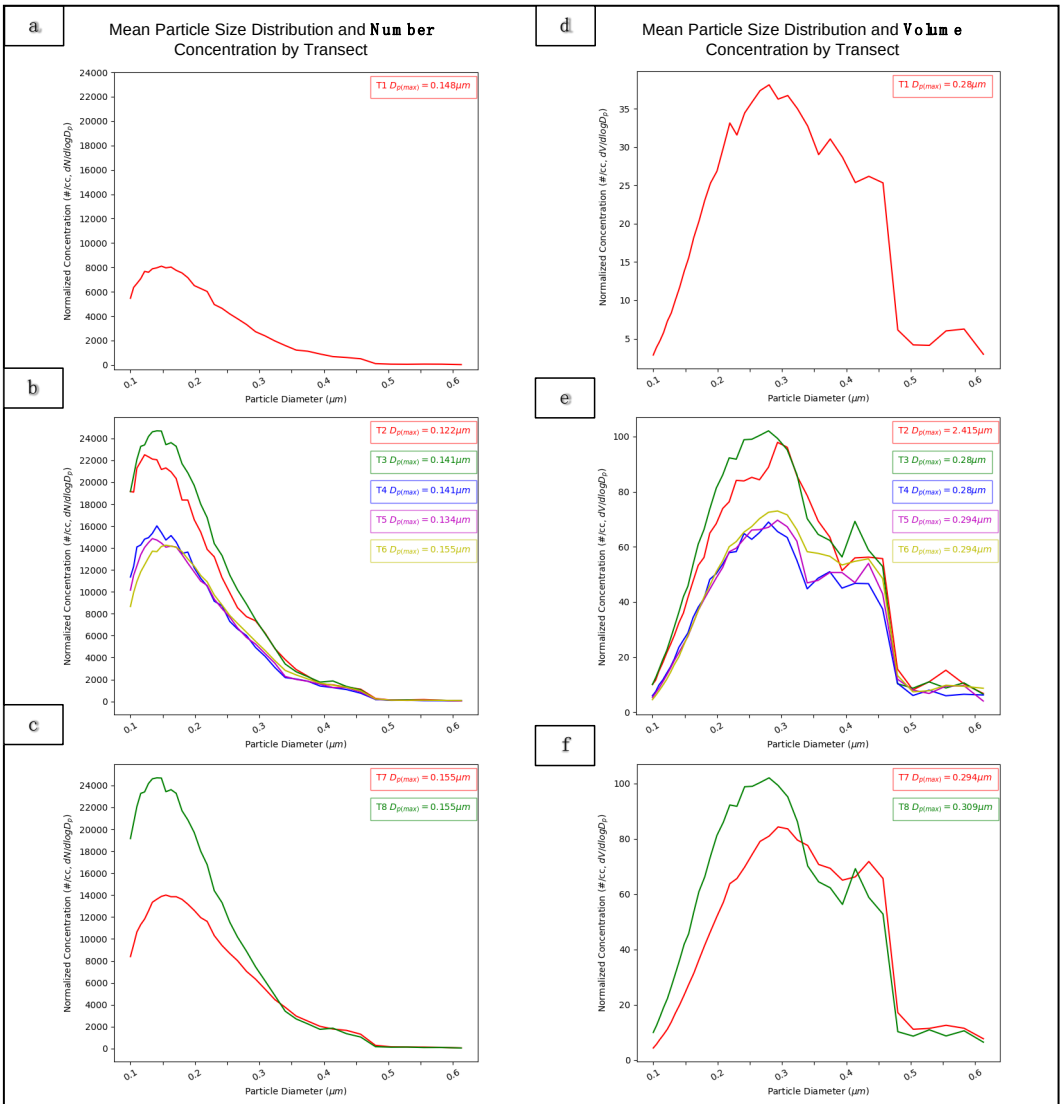

Figure 9. Mean particle number (**a**–**c**) and volume (**d**–**f**) concentrations and size distributions for each transect observed by the FIREX aircraft (from the LAS instrument), where (**a**) includes transect 1 and samples the downwind end of Region I, (**b**) includes transects 2 through 6, corresponding to Region II, and (**c**) contains transects 7 and 8 that observed Region III. The mode aerosol diameter for each transect is provided as well, where box and text color are matched with the corresponding transect color.

3.2.1. Overview of Comparison

The DIAL-HSRL aerosol backscatter at 532 nm illustrates the evolving vertical plume dynamics as the day progressed during FIREX sampling. The smoke layer was confined mostly below 2 km ASL during the first longitudinal overpass (L1) at ~19:00 UTC (Figure 6), consistent with the plume heights retrieved by MISR/MINX at approximately the same time. During L2, at ~20:30 UTC, the plume rose above 3 km, reaching as high as 4.0 km for L3 at ~21:50 UTC. This reflects typical diurnal fire behavior; burning often increases in intensity in the afternoon as temperatures rise and relative humidity decreases, amplifying smoke plume vertical and horizontal extent. Horizontal wind speeds measured by the DC-8 are relatively consistent with the MINX-retrieved wind speeds a few hours earlier. Furthermore, for the entire plume, there is a systematic decrease in the MISR AOD with downwind distance, which is confirmed by aircraft particle concentration measurements from FIREX. Lastly, inversions from the AERONET DRAGON [77] mobile photometers deployed during FIREX show particle mid-visible SSA of 0.94 and ANG of 1.74 measured in the plume vicinity. Though not

within the plume as observed by MISR due to differences in the times of observation, these are consistent with the retrieved size and absorption measurements from both MISR and the DC-8 instruments.

Table 2. Aircraft-measured particle properties, averaged by transect. Norm.– CO-normalized.

Transect	Age [a]	MCE	Peak D_p [b]	$D_{(10\%)}$ [c]	$D_{(50\%)}$ [d]	$D_{(90\%)}$ [e]	Aerosol Count [f]	Norm. Aerosol Count [g]
1	32.67	0.874	0.148	<0.105	0.155	0.266	157,122	682.192
2 [p]	45.59	0.896	0.122	<0.105	0.148	0.254	421,668	1030.10
3	60.85	0.898	0.141	<0.105	0.155	0.254	466,133	1024.62
4	84.89	0.931	0.141	<0.105	0.155	0.254	295,146	907.454
5	112.8	0.887	0.134	<0.105	0.155	0.266	284,720	844.080
6	115.6	0.892	0.155	<0.105	0.163	0.266	279,631	853.498
7	142.9	0.899	0.155	0.11	0.163	0.28	286,611	855.151
8	n/a	0.814	0.155	0.11	0.171	0.294	236,239	734.102

Transect	BC [h]	Norm. BC [i]	CCN [j]	Norm. CCN [k]	Oxidation [l]	SSA_{530} [m]	Norm. BrC Absorption [n]	Norm. BC Absorption [o]
1	417.9	1.258	3619	11.98	0.3730	0.928	0.0565	0.0217
2	1413	2.899	7358	16.03	0.3236	0.927	0.0783	0.0371
3	1673	3.587	8712	18.86	0.3806	0.923	0.0850	0.0403
4	1151	3.469	5482	16.78	0.5498	0.928	0.0679	0.0358
5	1120	3.338	5377	15.78	0.6299	0.934	0.0632	0.0297
6	951.9	2.880	6567	19.89	0.6478	0.929	0.0718	0.0276
7	898.4	2.684	6252	18.17	0.7339	0.936	0.0702	0.0267
8	826.2	2.512	5110	15.68	0.6867	0.942	0.0662	0.02032

[a] Estimated age of smoke measured in each transect in minutes, calculated based on aircraft-measured wind speed; [b] Bin size at which the transect-averaged particle size distribution peaks in μm (the mode aerosol size), as measured by the LAS instrument; [c] The diameter (μm) below which 10% of the total measured aerosol population exists, as measured by the LAS instrument; [d] The diameter (μm) below which 50% of the total measured aerosol population exists, as measured by the LAS instrument; [e] The diameter (μm) below which 90% of the total measured aerosol population exists, as measured by the LAS instrument; [f] The total concentration of aerosols (#/cc) as measured by the LAS instrument; [g] The ratio of the total aerosol count from the LAS instruments (#/cc) and the CO concentration measured by DACOM instrument (ppb); [h] Mass concentration of BC measured by the SP2, in ng/std.m^3; [i] The ratio of BC mass concentration (ng/std.m^3) from the SP2 and CO measured by DACOM instrument (ppb); [j] The concentration (#/cc) of CCN that activated at 0.34% superstation, as measured by the CCN-100; [k] The ratio of CCN measured by the CCN-100 instrument (#/cc) and CO measured by DACOM instrument (ppb); [l] Defined as $-\mathrm{Log}[NO_x/NO_y]$, using measurements provided by the ozone-induced chemiluminescence technique, where 0 is interpreted as fresh smoke and 1 is aged smoke; [m] As measured by the PSAP/neph; [n] The residual of the ratio of 405 nm absorption (PAS; Mm^{-1}) and CO concentration (DACOM; ppb) and the ratio of 664 nm absorption (PAS; Mm^{-1}) and CO concentration (DACOM; ppb); [o] The ratio of 664 nm absorption (PAS; Mm^{-1}) and CO concentration (DACOM; ppb); [p] The point at which the southern and northern plume merge in the aircraft data.

In both the FIREX- and MISR-observed plume, particle absorption systematically decreases downwind, although the spread of SSA values is considerably smaller in the FIREX observations. There is also a clear favoring of BC from the southeast hotspot compared to the northwest hotspot in both datasets; for FIREX, this is evident from the large injection of absolute and dilution-corrected BC mass concentrations at the point of convergence between the two plumes (Table 2), whereas for MISR this is evident from the consistently elevated BC analog AOD throughout the length of the southern plume compared to the northern plume. Both sets of observations also indicate there is at least some presence of a spectrally steep light-absorbing component, with a varying level of contribution to the total absorption; for FIREX, this is evident from the differences in absorption at the long and short end of the visible spectrum as measured by PAS (Table 2), and for MISR this appears from the localized area of BrC-like particles along the northern edge of Region II.

MISR indicates a significant presence of non-spherical aerosols along the northern plume boundary in Region II as well as in the surrounding background air. Although the in situ aerosol depolarization measurements are dominated by values reflective of less depolarizing biomass burning aerosols (between 3–6%) within the plume, larger depolarization values just outside the plume reflect the presence of at least some background dust (bottom row of Figure 6, at ~20.65–20.66 and 21.94–21.95 h). It is also possible that MISR retrieves these non-spherical particles because they offer the best match in the RA climatology to the actual particle size, rather than due to matching particle shape (Table S1 in the Supplementary Materials). Furthermore, the sporadic nature of aircraft sampling and the time difference between the satellite and aircraft observations may contribute to the apparent discrepancy.

Table 3. Aircraft data aggregated by plume region: aerosol size, chemical, and physical properties for the Williams Flats Fire measured in situ on 06 August 2019. Norm.– CO-normalized.

Plume Region:		Near-Source (Region I)	Mid-Plume (Region II)	Downwind (Region III)
Very small Aerosols [a]	Mean	0.626	0.617	0.553
	±σ	±0.0218	±0.0298	±0.0173
	Median	0.632	0.611	0.550
Small Aerosols [a]	Mean	0.298	0.312	0.348
	±σ	±0.0166	±0.0211	±0.00883
	Median	0.297	0.318	0.349
Medium Aerosols [a]	Mean	0.0732	0.0678	0.0979
	±σ	±0.00912	±0.0101	±0.00970
	Median	0.0718	0.0696	0.0968
Large Aerosols [a]	Mean	0.0000458	0.0000567	0.000172
	±σ	±0.000102	±0.0001151	±0.000137
	Median	0	0	0.000221
SSA_{530} [b]	Mean	0.924	0.929	0.939
	±σ	±0.042	±0.0112	±0.00577
	Median	0.937	0.932	0.939
Oxidation [c]	Mean	0.354	0.526	0.711
	±σ	±0.0930	±0.158	±0.0540
	Median	0.360	0.552	0.707
BC Mass Concentration [d]	Mean	591.7	1187	855.0
	±σ	±936.8	±630.9	±247.5
	Median	184.8	1058	788.0
Norm. BC Mass Concentration [e]	Mean	1.30	3.10	2.56
	±σ	±0.729	±0.890	±0.233
	Median	1.07	3.11	2.52
CCN [f]	Mean	4081	6594	5728
	±σ	±5898	±3344	±1669
	Median	1620	6364	5477
Norm. CCN Concentration [g]	Mean	11.2	17.3	17.1
	±σ	±6.35	±4.34	±1.68
	Median	9.78	17.2	16.8
Norm. Total Aerosol Count [h]	Mean	547.1	903.1	800.0
	±σ	±227.1	±229.3	±102.9
	Median	509.9	882.1	808.1

[a] Fraction of total aerosol count, as measured by the LAS instrument; [b] As measured by the PSAP/neph; [c] Defined as $-\text{Log}[NO_x/NO_y]$, using measurements provided by the ozone-induced chemiluminescence technique, where 0 is interpreted as fresh smoke and 1 is aged smoke; [d] As measured by the SP2, in ng/std.m^3; [e] The ratio of BC mass concentration (ng/std.m^3) from the SP2 and CO measured by the DACOM instrument (ppb); [f] The concentration (#/cc) of CCN that activated at 0.34% superstation, as measured by the CCN-100; [g] The ratio of CCN measured by the CCN-100 instrument (#/cc) and CO measured by the DACOM instrument (ppb); [h] The ratio of the total aerosol count from the LAS instruments (#/cc) and the CO concentration measured by the DACOM instrument (ppb).

Particles are overall fine at both times of observation, with slightly increasing size with age at least through Region II. However, MISR-retrieved REPS suggests decreasing particle size in Region III, whereas the aircraft shows continued increases in size (Table 2, Figure 8). Moreover, MISR indicates that particle size is increasingly dominated by "medium" aerosol fractions in Regions II and III, and although the aircraft measurements do exhibit increased fractions of aerosols in this size range (excluding in Transect 2, which brings down the regional average), overall aerosol size is comparatively more firmly rooted in the "small" and "very small" size categories (Figure 8, Table 3). However, both the in situ and MISR observations suggest smaller particles from the southeast hotspot; for FIREX, this is evident from the decreased particle size at the point of convergence between the two plumes, whereas for MISR this is evident from the consistently smaller particles throughout the length of the southern plume compared to the northern plume. The lidar 1064/532 nm color ratio is typical of values for BB plumes, but does not reflect the downwind increases in particle size observed by

MISR and by the in situ LAS instrument, likely due to sensitivity limitations in the color ratio itself. (Although transect-by-transect changes in the LAS are small, they are systemic and significant when taken over the whole plume). The apparent differences between MISR and the in situ size distributions in Regions II and III might be due to larger particles preferentially settling downward in the plume, as the aircraft samples at a single elevation whereas MISR REPS represents the entire vertical column (this is discussed further in Section 3.2.2).

The in situ observations provide some further constraints on particle properties that cannot be directly measured by satellite observations, such as oxidation state and particle hygroscopicity. The plume clearly becomes increasingly oxidized with downwind distance (Figure 7b); however, it does not exhibit significant increases in particle hygroscopicity except in Region II, where the aircraft also observed enhanced BrC absorption (Figure 7f, Table 2). Furthermore, the lidar ratio, which typically provides information on particle composition, steadily increases downwind (Figures S8, S9, and S11), consistent with values observed for fresh smoke [62]. (Interpretation of the lidar ratio is ambiguous in this case; see Supplementary Materials for further discussion of the lidar measurements.)

3.2.2. Connecting Downwind Plume Changes between MISR and FIREX

The aircraft data generally support the observed trends in MISR REPS and REPA as well as the general MISR particle type retrievals, as discussed above. In this section, we explore in further detail the relationships between the FIREX observations and the satellite-inferred aging mechanisms introduced in Section 3.1.

Because smoke from the southeast hotspot was not sampled during Transect 1 (T1), and smoke from both hotspots converged downwind, there are key differences in the aircraft-observed particle properties between the first two transects that may be attributed to differences in near-source emissions. As seen in Table 2, this is supported by: (1) lower average oxidation in Transect 2 (T2), as the sampling location is nearer the southeast hotspot, providing generally fresher smoke; (2) dramatically larger aerosol and CCN number concentrations in T2, indicating higher rates of particle production from the southeast hotspot; (3) dramatically larger absolute and dilution-corrected BC mass concentration in T2, indicating differential BC emissions relative to CO emissions between the two hotspots (this is further supported by larger CO-normalized BC-only absorption as well as larger MCE); and (4) a particle size distribution in T2 that is both narrower in range and skewed towards comparatively smaller particles compared to T1, as fresh smoke is usually smaller in size. These aircraft-derived differences in particle properties are also seen directly in the MISR retrievals by comparing Region IV results with Regions I-III. As such, the in situ measurements support the inferred Mechanism (4) presented in Section 3.1. As mentioned in the discussion of the satellite results, the southern plume region is on average dominated by particles that are overall smaller and more BC-like than those retrieved in the northern plume, indicating that the differences in the dominant emitted particle types between the two hotspots exist at both times of observation (~ 2 h apart). The emission differences may be due to differences in the vegetation burning in each hotspot: MODIS IGBP land cover suggests the northwest hotspot is burning in areas with relatively larger fractions of evergreen forest, whereas fuel in the southeast hotspot is mostly savanna and grassland. Finer grass-like fuels tend to produce larger fractions of BC particles than fuels with coarser materials such as wood found in forest. However, the difference in particle type may also be due to differences in elevation between the two hotspots, as fires burning uphill (in this case, the southern plume) tend to burn more quickly. Therefore, smoke in the southern plume may be fresher on average than smoke in the northern plume, resulting in higher fractions of BC. Lastly, wind speeds in the southern plume are somewhat faster, at least at the time of MISR observation (on average 4.26 ± 1.66 m/s vs. 3.88 ± 1.96 m/s; Figure S1 in the Supplementary Materials), further suggesting that the southeast plume smoke may be fresher. In the case of FIREX, there continues to be generally high BC mass for the first three transects, indicative of the increased level of mixing between the northern and southern components. This mixing blurs the division between "near-source" and "mid-plume" regions as defined in the MISR plume.

In Region II, particle size steadily increases from T3 onward, supporting the observed trends in particle size observed by MISR. The increased oxidation levels in T3 and subsequent transects suggest that the increase in aerosol size may be due to the condensation of VOCs onto particle surfaces as plume aging progresses. Coagulation may also play a role, at least in T3, where the increase in particle size is accompanied by a decrease in the normalized aerosol concentration compared to T2. This could be attributed to ultrafine particles below the detection limit of the LAS and SP2 (~0.09 μm) aggregating to form larger particles or coagulating onto existing ones, although this is not directly testable with available data. It is possible that a combination of coagulation and VOC condensation is occurring. The trends in particle size and oxidation here support inferred Mechanism (1) in Section 3.1.

The FIREX- and MISR-observed trends in particle size diverge in Region III, with in situ observations suggesting continued increases in size, whereas the satellite suggests particle size begins to decrease here. As mentioned above, this may be explained by the differences in vertical sampling, as the aircraft measures at a single altitude, whereas MISR observes the entire column. Column aerosol loading is dominated by the smoke plume in this case, but the plume is at least 0.75 km thick (Figure 2b); thus, aircraft measurements at a single elevation might not be representative if particles are size-sorted in the vertical. In Region II, the "large" aerosols observed by MISR may have preferentially settled below the altitude of aircraft sampling, and then proceeded to settle out of the column entirely in Region III, deposited onto the surface at approximately 40 km downwind, where the plume extent reaches the surface (Figure 2b). This would explain both the differences in satellite and in situ size observations, as well as the along-plume changes in particle size observed by MISR. As such, we conclude that gravitational settling of larger particles may play a role downwind of the source, as suggested by Mechanism (2) in Section 3.1.

Both MISR and FIREX suggest decreasing particle light-absorption and a loss of BC particles with smoke age. The variations in SSA over the aircraft transects, on the order of ±0.005, are probably within the range of measurement uncertainty. However, SSA appears to systematically decrease by region on average, with the exception of T2 and T3, which are more similar to T1 than the other Region II transects (possibly due to the injection of fresh BC particles at these points from the southeast hotspot). Furthermore, the spectral dependence of PAS absorption measurements suggests that absorption due to BC (i.e., the absorption measured at 664 nm) systematically decreases throughout Regions II and III; the SP2-measured BC mass concentration similarly decreases. The steadily increasing level of oxidation observed in situ corresponds with these changes, supporting the inferred Mechanism (3) in Section 3.1.

3.3. An Improved Understanding of MISR Capabilities

Although an independent study, the investigation described here builds directly upon Paper 1. In both cases where near-coincident data were acquired, MISR particle properties reflect the systematic oxidation of particles with downwind distance, transitioning from highly light-absorbing particles near the source to non-absorbing particles downwind. In addition, in both studies, trends in retrieved particle size can be linked, to a significant degree, to the relative influences of condensational growth, particle coagulation, secondary particle formation, and size-selective gravitational settling. In Paper 1, decreasing particle size was correlated with the formation of new organic (brown carbon) aerosols as well as a possible loss of larger-size particles from the column, whereas increasing size was attributed to a combination of hydration, condensation, and aggregation. In the current study, decreasing particle size is similarly connected to the preferential settling of large particles, but significant new particle formation was not observed. Instead, the injection of fresh, very small particles from a different source (the southern plume) drove decreasing particle size slightly downwind. The ability to distinguish particle properties between two adjacent sources and observe how the emissions interact downwind is a unique contribution demonstrated for the first time in the current study. Furthermore, linking these differences to observed variations in fuel characteristics and topography increases confidence in our interpretation of differences in MISR-retrieved smoke particle properties. In the same vein, the presence of non-spherical particles in the Williams Flats plume was at least somewhat confirmed by lidar data

that was unavailable for Paper 1. Further, the lidar validated the plume heights retrieved by MISR, and documented the changes between the MISR overpass and subsequent aircraft sampling.

4. Conclusions

There are distinct differences in particle size and light-absorption properties in different regions of the Williams Flats Fire plume on 06 August 2013, as observed by MISR. Overall, the satellite-retrieved particle properties indicate that the plume contained fine, highly absorbing, BC-like aerosols near the source, whereas downwind, the plume tends to show a systematically increasing amount and fraction of weakly absorbing, less BC-like aerosols. Furthermore, MISR suggests particles increase in size between ~30 and 140 min of aging, but decrease in size for smoke older than about 140 min. These observations are relatively well supported by near-coincident FIREX-AQ in situ observations, with minor disparities that fall within measurement uncertainty and/or sampling differences.

Due to the comprehensive coverage, the MISR observations provide greater context for the particle properties observed in situ; this additional information allows us to paint a more complete picture of plume mechanics and particle aging. Specifically, from MISR-retrieved plume height, REPS, REPA, and SSA spectral dependence, we infer (1) VOC condensation and possibly coagulation occur between ~30 and 140 min of aging (Region II of Figure 1), (2) gravitational settling and/or dilution alter vertically resolved particle size as the smoke ages beyond about 140 min (Region III), (3) particles on average become progressively more oxidized downwind along the entire plume, and (4) the southeast hotspot (Region IV) generates more smoke, a larger fraction of BC, and generally smaller particles than the northwest hotspot. The FIREX-AQ in situ observations also largely support these inferences, as summarized in Section 3.2.2 above.

The FIREX data allow us to investigate the strengths and limitations of using satellite data for characterizing wildfire smoke plume extent and particle characteristics. As in Paper 1, where near-coincident data were acquired, the MISR-retrieved information on particle size and absorption matches that observed in situ, showing similar patterns with age. The combined results from these studies provides extensive validation of several key smoke-plume properties not previously obtained from remote sensing. In the future, such data can be used to help refine climate modeling of wildfire smoke-related processes. The MISR RA results are also useful as a supplement to near-coincident observations, as they place the aircraft observations in a broader context and offer more comprehensive coverage of the plume. Satellite data provide the necessary information to derive relationships among plume elements of varying ages, making it possible to infer the active mechanisms driving particle evolution.

This study expands upon the validation work conducted in Paper 1. We introduce a suite of new aircraft data and modeling, which further test our interpretation of the relationships between fire chemistry/dynamics and the particle properties observed from space. The results build upon the previous study, demonstrating reproducibility and bolstering our confidence in RA performance. As in Paper 1, MISR tends to observe somewhat higher contributions from relatively larger size categories compared to the aircraft data, and in both validation studies, these larger particles appear to experience size-selective gravitational settling downwind. Both studies also suggest that coagulation and condensation affect REPS, and oxidation plays a large role in particle REPA.

As the MISR data record contains global coverage about once per week for over 20 years, there is a vast trove of smoke-plume observations available for further study. Future work will involve applying MISR plume height and particle property retrievals to a wide range of biomass burning events where in situ observations are lacking. Statistical analysis of plume particle properties from a large suite of cases, focusing on the apparent changes in particle size, SSA, and SSA spectral dependence, should improve our understanding of: (1) the relationships between the characteristics of wildfire smoke sources and the resulting emissions, and (2) the conditions that lead to the occurrence of different aging mechanisms both within and between smoke plumes. Such insight represents new territory in aerosol science and may help improve climate and air quality modeling.

Supplementary Materials: The following are available online at http://www.mdpi.com/2072-4292/12/22/3823/s1: Figure S1: MISR-MINX Wind Trajectories for the Williams Flats Fire; Figure S2: Relative Humidity for the Williams Flats Fire; Figure S3: Transect Key for the Williams Flats Fire; Table S1: MISR RA Climatology; Figure S4: DIAL-HSRL Volume and Aerosol Depolarization for L1; Figure S5: DIAL-HSRL Volume and Aerosol Depolarization for L2; Figure S6: DIAL-HSRL Volume and Aerosol Depolarization for Transverse Transects; Figure S7: DIAL-HSRL Volume and Aerosol Depolarization for L3; Figure S8: DIAL-HSRL Lidar and Color Ratios for L1; Figure S9: DIAL-HSRL Lidar and Color Ratios for L2; Figure S10: DIAL-HSRL Lidar and Color Ratios for Transverse Transects; Figure S11: DIAL-HSRL Lidar and Color Ratios for L3; Figure S12: DIAL-HSRL Volume and Aerosol Depolarization Variability for L1; Figure S13: DIAL-HSRL Volume and Aerosol Depolarization Variability for L2; Figure S14: DIAL-HSRL Volume and Aerosol Depolarization Variability for Transverse Transects; Figure S15: DIAL-HSRL Volume and Aerosol Depolarization Variability for L3; Figure S16: DIAL-HSRL Lidar and Color Ratios Variability for L1; Figure S17: DIAL-HSRL Lidar and Color Ratios Variability for L2; Figure S18: DIAL-HSRL Lidar and Color Ratios Variability for Transverse Transects; Figure S19: DIAL-HSRL Lidar and Color Ratios Variability for L3.

Author Contributions: The project was first conceptualized by R.A.K, and the development and design of the methodology were a collaboration between R.A.K. and K.T.J.N. The RA algorithm used in this project was developed by R.A.K. and J.A.L., and is maintained by J.A.L. K.T.J.N. developed the tools used to analyze and visualize the results of both the RA and in situ data (with the exception of the lidar curtains in Figure 6). Formal analysis of the satellite results and the majority of the in situ results was conducted by K.J.N and R.A.K., who together wrote the original draft. J.W.H., T.J.S. and M.A.F. provided the DIAL-HSRL data and conducted the formal lidar analysis, and T.J.S. produced the lidar curtain figure. T.J.S., J.W.H., and M.A.F. reviewed and edited the lidar-related discussion. R.H.M., E.L.W., C.E.R., K.J.S., K.L.T., and E.B.W. contributed their data from the LAS, CCN, and PSAP/neph instruments and provided comments on the manuscript. D.M.G. contributed the AERONET DRAGON data and provided comments on the manuscript. J.M.K. contributed data from the SP2 and provided comments on the manuscript. Z.L. reviewed and provided comments on the manuscript. All authors have read and agreed to the final version of the manuscript.

Funding: The work of K.T. Junghenn Noyes is supported in part by a grant from the Maryland Space Grant Consortium under Richard C. Henry and Matt Collinge, as well as NASA's Atmospheric Composition Modeling and Analysis Program under Richard Eckman through a grant to R. Kahn, and a NASA grant (NNX16AN61G) that supports Zhanqing Li. The work of R.A. Kahn is supported in part by NASA's Climate and Radiation Research and Analysis Program under Hal Maring, NASA's Atmospheric Composition Modeling and Analysis Program under Richard Eckman, and the EOS Terra and MISR Projects. The Langley Aerosol Research Group (LARGE) group is supported by the NASA Tropospheric Chemistry Program (managed by Dr. Barry Lefer). E. Wiggins and K. Sanchez are supported in part through the NASA Postdoctoral Program. David Giles is supported by the Earth Observing System Project Science Office cal-val, the Radiation Sciences Program at NASA headquarters, and various field campaigns.

Acknowledgments: The authors thank NASA for the support to participate in the FIREX-AQ campaign under Barry Lefer, and both NASA and NOAA for supporting the aircraft data. We also thank the FIREX instrument PIs and their teams, listed as follows:

- DACOM: Glenn Diskin, Joshua DiGangi, John Nowak, Hannah Halliday, James Geiger, Johnny Mau, James Plant, Mario Rana, and Yoonghoon Choi (NASA LaRC)
- SP2: Joshua Schwarz, Laurel Watts, (NOAA ESRL), Anne Perring, and Brady Mediavilla, (Colgate University)
- PAS: Nick Wagner, Adam Ahern, Charles Brock (NOAA ESRL), and Ming Lyu (University of Alberta)
- Nitrogen Oxides: Jeff Peischl, Tom Ryerson, (NOAA ESRL) and Ilann Bourgeois (CIRES).
- AERONET: Brent Holben and the AERONET team participating from NASA GSFC and the University of Lille/LOA (PHOTONS)

Joshua Schwarz provided the calculations of MCE and transect age. Joseph Katich is a member of the SP2 team (NASA Langley Research Center). Richard Moore, Elizabeth Wiggins, Edward Winstead, Claire Robinson, Lee Thornhill, and Kevin Sanchez are members of the Langley Aerosol Research Group Experiment (LARGE) team (CCN-100, LAS, PSAP/neph; NASA Langley Research Center). David Giles is a member of the AERONET team. We also thank Amber Soja (NASA Langley Research Center) for data on the FCCS fuels burned in the Williams Flats plume.

Conflicts of Interest: The authors declare no conflict of interest.

References

1. Bond, T.C.; Doherty, S.J.; Fahey, D.W.; Forster, P.M.; Berntsen, T.; DeAngelo, B.J.; Flanner, M.G.; Ghan, S.; Kaercher, B.; Koch, D.; et al. Bounding the role of black carbon in the climate system: A scientific assessment. *J. Geophys. Res. Atmos.* **2013**, *118*, 5380–5552. [CrossRef]
2. Feng, Y.; Ramanathan, V.; Kotamarthi, V.R. Brown Carbon: A Significant Atmospheric Absorber of Solar Radiation? *Atmos. Chem. Phys.* **2013**, *13*, 8607–8621. [CrossRef]

3. Koch, D.; Del Genio, A.D. Black carbon semi-direct effects on cloud cover: Review and synthesis. *Atmos. Chem. Phys.* **2010**, *10*, 7685–7696. [CrossRef]
4. Colarco, P.R.; Schoeberl, M.R.; Doddridge, B.G.; Marufu, L.T.; Torres, O.; Welton, E.J. Transport of Smoke from Canadian Forest Fires to the Surface near Washington, D.C.: Injection Height, Entrainment, and Optical Properties. *J. Geophys. Res.* **2004**, *109*. [CrossRef]
5. Kahn, R.A.; Chen, Y.; Nelson, D.L.; Leung, F.-Y.; Li, Q.; Diner, D.J.; Logan, J.A. Wildfire Smoke Injection Heights: Two Perspectives from Space. *Geophys. Res. Lett.* **2008**, *35*, L04809. [CrossRef]
6. Warner, J.; Twomey, S. The Production of Cloud Nuclei by Cane Fires and the Effect on Cloud Droplet Concentration. *J. Atmos. Sci.* **1967**, *24*, 704–706. [CrossRef]
7. Hobbs, P.V.; Radke, L.F. Cloud Condensation Nuclei from a Simulated Forest Fire. *Science* **1969**, *163*, 279–280. [CrossRef]
8. Hansen, J.; Sato, M.; Ruedy, R. Radiative forcing and climate response. *J. Geophys. Res.* **1997**, *102*. [CrossRef]
9. Dubovik, O.; Holben, B.; Eck, T.F.; Smirnov, A.; Kaufman, Y.J.; King, M.D.; Tanre, D.; Slutsker, I. Variability of Absorption and Optical Properties of Key Aerosol Types Observed in Worldwide Locations. *J. Atmos. Sci.* **2002**, *59*, 19. [CrossRef]
10. Chen, W.-T.; Kahn, R.A.; Nelson, D.; Yau, K.; Seinfeld, J.H. Sensitivity of Multiangle Imaging to the Optical and Microphysical Properties of Biomass Burning Aerosols. *J. Geophys. Res.* **2008**, *113*, D10203. [CrossRef]
11. Eck, T.F.; Holben, B.N.; Reid, J.S.; O'Neill, N.T.; Schafer, J.S.; Dubovik, O.; Smirnov, A.; Yamasoe, M.A.; Artaxo, P. High Aerosol Optical Depth Biomass Burning Events: A Comparison of Optical Properties for Different Source Regions. *Geophys. Res. Lett.* **2003**, *30*. [CrossRef]
12. Shi, S.; Cheng, T.; Gu, X.; Guo, H.; Wu, Y.; Wang, Y. Biomass Burning Aerosol Characteristics for Different Vegetation Types in Different Aging Periods. *Environ. Int.* **2019**, *126*, 504–511. [CrossRef] [PubMed]
13. Reid, J.S.; Hobbs, P.V. Physical and optical properties of young smoke from individual biomass fires in Brazil. *J. Geophys. Res.* **1998**, *103*. [CrossRef]
14. Reid, J.S.; Koppmann, R.; Eck, T.F.; Eleuterio, D.P. A Review of Biomass Burning Emissions Part II: Intensive Physical Properties of Biomass Burning Particles. *Atmos. Chem. Phys.* **2005**, *28*, 799–825. [CrossRef]
15. Chakrabarty, R.K.; Moosmüller, H.; Chen, L.-W.A.; Lewis, K.; Arnott, W.P.; Mazzoleni, C.; Dubey, M.K.; Wold, C.E.; Hao, W.M.; Kreidenweis, S.M. Brown Carbon in Tar Balls from Smoldering Biomass Combustion. *Atmos. Chem. Phys.* **2010**, *10*, 6363–6370. [CrossRef]
16. Chakrabarty, R.K.; Gyawali, M.; Yatavelli, R.L.N.; Pandey, A.; Watts, A.C.; Knue, J.; Chen, L.-W.A.; Pattison, R.R.; Tsibart, A.; Samburova, V.; et al. Brown Carbon Aerosols from Burning of Boreal Peatlands: Microphysical Properties, Emission Factors, and Implications for Direct Radiative Forcing. *Atmos. Chem. Phys.* **2016**, *16*, 3033–3040. [CrossRef]
17. Petrenko, M.; Kahn, R.; Chin, M.; Soja, A.; Kucsera, T.; Harshvardhan. The Use of Satellite-Measured Aerosol Optical Depth to Constrain Biomass Burning Emissions Source Strength in the Global Model GOCART. *J. Geophys. Res.* **2012**, *117*. [CrossRef]
18. Kirchstetter, T.W.; Novakov, T.; Hobbs, P.V. Evidence that the spectral dependence of light absorption by aerosols is affected by organic carbon. *J. Geophys. Res. Atmos.* **2004**, *109*, D21208. [CrossRef]
19. Samset, B.H.; Stjern, C.W.; Andrews, E.; Kahn, R.A.; Myhre, G.; Schulz, M.; Schuster, G.L. Aerosol Absorption: Progress Towards Global and Regional Constraints. *Curr. Clim. Change Rep.* **2018**, *4*, 65–83. [CrossRef]
20. Zhou, S.; Collier, S.; Jaffe, D.A.; Briggs, N.L.; Hee, J.; Sedlacek, A.J., III; Kleinman, L.; Onasch, T.B.; Zhang, Q. Regional Influence of Wildfires on Aerosol Chemistry in the Western US and Insights into Atmospheric Aging of Biomass Burning Organic Aerosol. *Atmos. Chem. Phys.* **2017**, *17*, 2477–2493. [CrossRef]
21. Yokelson, R.J.; Crounse, J.D.; DeCarlo, P.F.; Karl, T.; Urbanski, S.; Atlas, E.; Campos, T.; Shinozuka, Y.; Kapustin, V.; Clarke, A.D.; et al. Emissions from Biomass Burning in the Yucatan. *Atmos. Chem. Phys.* **2009**, *28*, 5785. [CrossRef]
22. Akagi, S.K.; Craven, J.S.; Taylor, J.W.; McMeeking, G.R.; Yokelson, R.J.; Burling, I.R.; Urbanski, S.P.; Wold, C.E.; Seinfeld, J.H.; Coe, H.; et al. Evolution of Trace Gases and Particles Emitted by a Chaparral Fire in California. *Atmos. Chem. Phys.* **2012**, *12*, 1397–1421. [CrossRef]
23. Hennigan, C.J.; Westervelt, D.M.; Riipinen, I.; Engelhart, G.J.; Lee, T.; Collett, J.L.; Pandis, S.N.; Adams, P.J.; Robinson, A.L. New particle formation and growth in biomass burning plumes: An important source of cloud condensation nuclei. *Geophys. Res. Lett.* **2012**, *39*, L09805. [CrossRef]

24. Ahern, A.T.; Robinson, E.S.; Tkacik, D.S.; Saleh, R.; Hatch, L.E.; Barsanti, K.C.; Stockwell, C.E.; Yokelson, R.J.; Presto, A.A.; Robinson, A.L.; et al. Production of secondary organic aerosol during aging of biomass burning smoke from fresh fuels and its relationship to VOC precursors. *J. Geophys. Res. Atmos.* **2019**, *124*, 3583–3606. [CrossRef]
25. Wang, Z.B.; Hu, M.; Yue, D.L.; He, L.Y.; Huang, X.F.; Yang, Q.; Zheng, J.; Zhang, R.Y.; Zhang, Y.H. New particle formation in the presence of a strong biomass burning episode at a downwind rural site in PRD, China. *Tellus B* **2013**, *65*, 19965. [CrossRef]
26. May, A.A.; Levin, E.J.T.; Hennigan, C.J.; Riipinen, I.; Lee, T.; Collett, J.L.; Jimenez, J.L.; Kreidenweis, S.M.; Robinson, A.L. Gas-particle partitioning of primary organic aerosol emissions: 3. Biomass burning. *J. Geophys. Res. Atmos.* **2013**, *118*, 11327–11338. [CrossRef]
27. Kleinman, L.I.; Sedlacek, A.J. *Biomass Burning Observation Project Science Plan*; DOE/SC-ARM; Brookhaven National Laboratory (BNL): Upton, NY, USA, 2013.
28. Kleinman, L.I.; Sedlacek, A.J. *Biomass Burning Observation Project (BBOP): Final Campaign Report*; DOE ARM Climate Research Facility: Washington, DC, USA, 2016.
29. Toon, O.B.; Maring, H.; Dibb, J.; Ferrare, R.; Jacob, D.J.; Jensen, E.J.; Luo, Z.J.; Mace, G.G.; Pan, L.L.; Pfister, L.; et al. Planning, Implementation, and Scientific Goals of the Studies of Emissions and Atmospheric Composition, Clouds and Climate Coupling by Regional Surveys (SEAC ^{4} RS) Field Mission. *J. Geophys. Res. Atmos.* **2016**, *121*, 4967–5009. [CrossRef]
30. Forrister, H.; Liu, J.; Scheuer, E.; Dibb, J.; Ziemba, L.; Thornhill, K.L.; Anderson, B.; Diskin, G.; Perring, A.E.; Schwarz, J.P.; et al. Evolution of Brown Carbon in Wildfire Plumes. *Geophys. Res. Lett.* **2015**, *42*, 4623–4630. [CrossRef]
31. Sedlacek, A.J., III; Buseck, P.R.; Adachi, K.; Onasch, T.B.; Springston, S.R.; Kleinman, L. Formation and Evolution of Tar Balls from Northwestern US Wildfires. *Atmos. Chem. Phys.* **2018**, *18*, 11289–11301. [CrossRef]
32. Adachi, K.; Sedlacek, A.J.; Kleinman, L.; Springston, S.R.; Wang, J.; Chand, D.; Hubbe, J.M.; Shilling, J.E.; Onasch, T.B.; Kinase, T.; et al. Spherical Tarball Particles Form through Rapid Chemical and Physical Changes of Organic Matter in Biomass-Burning Smoke. *Proc. Natl. Acad. Sci. USA* **2019**, *116*, 19336–19341. [CrossRef]
33. Jethva, H.; Torres, O. Satellite-Based Evidence of Wavelength-Dependent Aerosol Absorption in Biomass Burning Smoke Inferred from Ozone Monitoring Instrument. *Atmos. Chem. Phys.* **2011**, *11*, 10541–10551. [CrossRef]
34. Konovalov, I.B.; Beekmann, M.; Berezin, E.V.; Formenti, P.; Andreae, M.O. Probing into the Aging Dynamics of Biomass Burning Aerosol by Using Satellite Measurements of Aerosol Optical Depth and Carbon Monoxide. *Atmos. Chem. Phys.* **2017**, *17*, 4513–4537. [CrossRef]
35. Junghenn Noyes, K.; Kahn, R.; Sedlacek, A.; Kleinman, L.; Limbacher, J.; Li, Z. Wildfire Smoke Particle Properties and Evolution, from Space-Based Multi-Angle Imaging. *Remote Sens.* **2020**, *12*, 769. [CrossRef]
36. Diner, D.J.; Beckert, J.C.; Reilly, T.H.; Bruegge, C.J.; Conel, J.E.; Kahn, R.A.; Martonchik, J.V.; Ackerman, T.P.; Davies, R.; Gerstl, S.A.W.; et al. Multi-Angle Imaging SpectroRadiometer (MISR) Instrument Description and Experiment Overview. *IEEE Trans.* **1998**, *36*, 1072–1087. [CrossRef]
37. Nelson, D.L.; Chen, Y.; Kahn, R.A.; Diner, D.J.; Mazzoni, D. Example Applications of the MISR INteractive EXplorer (MINX) Software Tool to Wildfire Smoke Plume Analyses. *Remote Sens. Fire Sci. Appl.* **2008**, *7089*, 708909. [CrossRef]
38. Nelson, D.; Garay, M.; Kahn, R.; Dunst, B. Stereoscopic Height and Wind Retrievals for Aerosol Plumes with the MISR INteractive EXplorer (MINX). *Remote Sens.* **2013**, *5*, 4593–4628. [CrossRef]
39. Val Martin, M.; Logan, J.A.; Kahn, R.A. Smoke Injection Heights from Fires in North America: Analysis of 5 Years of Satellite Observations. *Atmos. Chem. Phys.* **2010**, *10*, 1491–1510. [CrossRef]
40. Val Martin, M.; Kahn, R.; Tosca, M. A Global Analysis of Wildfire Smoke Injection Heights Derived from Space-Based Multi-Angle Imaging. *Remote Sens.* **2018**, *10*, 1609. [CrossRef]
41. Scollo, S.; Kahn, R.A.; Nelson, D.L.; Coltelli, M.; Diner, D.J.; Garay, M.J.; Realmuto, V.J. MISR Observations of Etna Volcanic Plumes. *J. Geophys. Res.* **2012**, *117*. [CrossRef]
42. Tosca, M.G.; Randerson, J.T.; Zender, C.S.; Nelson, D.L.; Diner, D.J.; Logan, J.A. Dynamics of Fire Plumes and Smoke Clouds Associated with Peat and Deforestation Fires in Indonesia. *J. Geophys. Res.* **2011**, *116*, D08207. [CrossRef]
43. Kahn, R.A.; Limbacher, J. Eyjafjallajökull Volcano Plume Particle-Type Characterization from Space-Based Multi-Angle Imaging. *Atmos. Chem. Phys.* **2012**, *12*, 9459–9477. [CrossRef]

44. Flower, V.J.B.; Kahn, R.A. Assessing the Altitude and Dispersion of Volcanic Plumes Using MISR Multi-Angle Imaging from Space: Sixteen Years of Volcanic Activity in the Kamchatka Peninsula, Russia. *J. Volcanal. Geoth. Res.* **2017**, *337*, 1–15. [CrossRef]
45. Flower, V.J.B.; Kahn, R.A. Distinguishing Remobilized Ash from Erupted Volcanic Plumes Using Space-Borne Multiangle Imaging: Remobilized Ash Plumes. *Geophys. Res. Lett.* **2017**, *44*, 10772–10779. [CrossRef] [PubMed]
46. Flower, V.J.B.; Kahn, R.A. Karymsky Volcano Eruptive Plume Properties Based on MISR Multi-Angle Imagery and the Volcanological Implications. *Atmos. Chem. Phys.* **2018**, *18*, 3903–3918. [CrossRef]
47. Flower, V.J.B.; Kahn, R.A. Interpreting the Volcanological Processes of Kamchatka, Based on Multi-Sensor Satellite Observations. *Remote Sens. Environ.* **2020**, *237*, 111585. [CrossRef]
48. Flower, V.J.B.; Kahn, R.A. The evolution of Iceland volcano emissions, as observed from space. *J. Geophys. Res.* **2020**, *125*, e2019JD031625. [CrossRef]
49. Yu, Y.; Kalashnikova, O.V.; Garay, M.J.; Lee, H.; Notaro, M. Identification and Characterization of Dust Source Regions Across North Africa and the Middle East Using MISR Satellite Observations. *Geophys. Res. Lett.* **2018**, *45*, 6690–6701. [CrossRef]
50. Vernon, C.J.; Bolt, R.; Canty, T.; Kahn, R.A. The Impact of MISR-Derived Injection Height Initialization on Wildfire and Volcanic Plume Dispersion in the HYSPLIT Model. *Atmos. Meas. Technol.* **2018**, *11*, 6289–6307. [CrossRef]
51. Limbacher, J.A.; Kahn, R.A. MISR Research-Aerosol-Algorithm Refinements for Dark Water Retrievals. *Atmos. Meas. Technol.* **2014**, *7*, 3989–4007. [CrossRef]
52. Limbacher, J.A.; Kahn, R.A. Updated MISR Over-Water Research Aerosol Retrieval Algorithm—Part 2: A Multi-Angle Aerosol Retrieval Algorithm for Shallow, Turbid, Oligotrophic, and Eutrophic Waters. *Atmos. Meas. Technol.* **2019**, *12*, 675–689. [CrossRef]
53. Kahn, R.A.; Gaitley, B.J.; Garay, M.J.; Diner, D.J.; Eck, T.; Smirnov, A.; Holben, B.N. Multiangle Imaging SpectroRadiometer global aerosol product assessment by comparison with the Aerosol Robotic Network. *J. Geophys. Res.* **2010**, *115*, D23209. [CrossRef]
54. Kahn, R.A.; Gaitley, B.J. An Analysis of Global Aerosol Type as Retrieved by MISR: MISR Aerosol Type. *J. Geophys. Res. Atmos.* **2015**, *120*, 4248–4281. [CrossRef]
55. Lee, J.; Hsu, N.C.; Sayer, A.M.; Bettenhausen, C.; Yang, P. AERONET-Based Nonspherical Dust Optical Models and Effects on the VIIRS Deep Blue/SOAR Over Water Aerosol Product: Dust Optical Models for Deep Blue/SOAR. *J. Geophys. Res. Atmos.* **2017**, *122*, 10384–10401. [CrossRef] [PubMed]
56. Andreae, M.O.; Gelencser, A. Black Carbon or Brown Carbon? The Nature of Light-Absorbing Carbonaceous Aerosols. *Atmos. Chem. Phys.* **2006**, *18*, 3419–3463. [CrossRef]
57. Roberts, J.; Trainer, M.; Murphy, D.; Brown, S.; Brewer, A.; Gao, R.-S.; Fahy, D. Fire Influence on Regional to Global Environments and Air Quality (FIREX-AQ): A NOAA/NASA Interagency Intensive Study of North American Fires. 2018. Available online: https://www.esrl.noaa.gov/csl/projects/firex-aq/whitepaper.pdf (accessed on 12 August 2020).
58. National Aeronautics and Space Administration. *FIREX-AQ Science Team: Fire Influence on Regional to Global Environments and Air Quality Campaign*; Data Set; NASA Langley Atmospheric Science Data Center DAAC: Hampton, VA, USA, 2019. [CrossRef]
59. Anderson, T.L.; Ogren, J.A. Determining Aerosol Radiative Properties Using the TSI 3563 Integrating Nephelometer. *Aerosol Sci. Technol.* **1998**, *29*, 57–69. [CrossRef]
60. Virkkula, A. Correction of the Calibration of the 3-wavelength Particle Soot Absorption Photometer (3λ PSAP. *Aerosol Sci. Technol.* **2010**, *44*, 706–712. [CrossRef]
61. Hair, J.W.; Hostetler, C.A.; Cook, A.L.; Harper, D.B.; Ferrare, R.A.; Mack, T.L.; Welch, W.; Izquierdo, L.R.; Hovis, F.E. Airborne High Spectral Resolution Lidar for profiling aerosol optical properties. *Appl. Opt.* **2008**, *47*, 6734–6752. [CrossRef]
62. Burton, S.P.; Ferrare, R.A.; Hostetler, C.A.; Hair, J.W.; Rogers, R.R.; Obland, M.D.; Butler, C.F.; Cook, A.L.; Harper, D.B.; Froyd, K.D. Aerosol classification using airborne High Spectral Resolution Lidar measurements—Methodology and examples. *Atmos. Meas. Tech.* **2012**, *5*, 73–98. [CrossRef]
63. Burton, S.P.; Ferrare, R.A.; Vaughan, M.A.; Omar, A.H.; Rogers, R.R.; Hostetler, C.A.; Hair, J.W. Aerosol classification from airborne HSRL and comparisons with CALIPSO vertical feature mask. *Atmos. Meas. Tech.* **2013**, *6*, 1397–1412. [CrossRef]

64. Burton, S.P.; Vaughan, M.A.; Ferrare, R.A.; Hostetler, C.A. Separating mixtures of aerosol types in airborne High Spectral Resolution Lidar data. *Atmos. Meas. Tech.* **2014**, *7*, 419–436. [CrossRef]
65. Burton, S.P.; Hair, J.W.; Kahnert, M.; Ferrare, R.A.; Hostetler, C.A.; Cook, A.L.; Harper, D.B.; Berkoff, T.A.; Seaman, S.T.; Collins, J.E.; et al. Observations of the spectral dependence of linear particle depolarization ratio of aerosols using NASA Langley airborne High Spectral Resolution Lidar. *Atmos. Chem. Phys.* **2015**, *15*, 13453–13473. [CrossRef]
66. Dalirian, M.; Ylisirniö, A.; Buchholz, A.; Schlesinger, D.; Ström, J.; Virtanen, A.; Riipinen, I. Cloud droplet activation of black carbon particles coated with organic compounds of varying solubility. *Atmos. Chem. Phys.* **2018**, *18*, 12477–12489. [CrossRef]
67. Rose, D.; Gunthe, S.S.; Mikhailov, E.; Frank, G.P.; Dusek, U.; Andreae, M.O.; Pöschl, U. Calibration and measurement uncertainties of a continuous-flow cloud condensation nuclei counter (DMT-CCNC): CCN activation of ammonium sulfate and sodium chloride aerosol particles in theory and experiment. *Atmos. Chem. Phys.* **2008**, *8*, 1153–1179. [CrossRef]
68. Moore, R.H.; Nenes, A.; Medina, J. Scanning Mobility CCN Analysis—A Method for Fast Measurements of Size-Resolved CCN Distributions and Activation Kinetics. *Aerosol Sci. Tech.* **2010**, *44*, 861–871. [CrossRef]
69. Sachse, G.W.; Hill, G.F.; Wade, L.O.; Perry, M.G. Fast-response, high-precision carbon monoxide sensor using a tunable diode laser absorption technique. *J. Geophys. Res.* **1987**, *92*, 2071–2081. [CrossRef]
70. Sachse, G.W.; Collins, J.E., Jr.; Hill, G.F.; Wade, L.O.; Burney, L.G.; Ritter, J.A. Airborne tunable diode laser sensor for high-precision concentration and flux measurements of carbon monoxide and methane. In Proceedings of the 4th Society of Photo-Optical Instrumentation Engineers (SPIE) International Symposium (OE/LASE '91), Los Angeles, CA, USA, 20–25 January 1991. [CrossRef]
71. Kleinman, L.I.; Springston, S.R.; Daum, P.H.; Weinstein-Lloyd, J.; Alexander, M.L.; Hubbe, J.; Ortega, J.; Canagaratna, M.R.; Jayne, J. The Time Evolution of Aerosol Composition over the Mexico City Plateau. *Atmos. Chem. Phys.* **2008**, *17*, 14461–14509. [CrossRef]
72. DeCarlo, P.F.; Dunlea, E.J.; Kimmel, J.R.; Aiken, A.C.; Sueper, D.; Crounse, J.; Wennberg, P.O.; Emmons, L.; Shinozuka, Y.; Clarke, A.; et al. Fast Airborne Aerosol Size and Chemistry Measurements above Mexico City and Central Mexico during the MILAGRO Campaign. *Atmos. Chem. Phys.* **2008**, *8*, 4027–4048. [CrossRef]
73. Ottmar, R.O. Smoke source characteristics. In *Smoke Management Guide for Prescribed and Wildland Fire*; National Interagency Fire Center: Boise, ID, USA, 2001; pp. 89–106. Available online: http://www.nwcg.gov/pms/pubs/SMG/SMG-72.pdf (accessed on 22 June 2020).
74. Urbanski, S.P. Combustion efficiency and emission factors for wildfire-season fires in mixed conifer forests of the northern Rocky Mountains, US. *Atmos. Chem. Phys.* **2013**, *13*, 7241–7262. [CrossRef]
75. InciWeb. Available online: https://inciweb.nwcg.gov/incident/6493/ (accessed on 12 August 2020).
76. Vay, S.A.; Woo, J.-H.; Anderson, B.E.; Thornhill, K.L.; Blake, D.R.; Westberg, D.J.; Kiley, C.M.; Avery, M.A.; Sachse, G.W.; Streets, D.G.; et al. Influence of regional-scale anthropogenic emissions on CO_2 distributions over the western North Pacific. *J. Geophys. Res.* **2003**, *108*, 8801. [CrossRef]
77. Holben, B.N.; Kim, J.; Sano, I.; Mukai, S.; Eck, T.F.; Giles, D.M.; Schafer, J.S.; Sinyuk, A.; Slutsker, I.; Smirnov, A.; et al. An overview of mesoscale aerosol processes, comparisons, and validation studies from DRAGON networks. *Atmos. Chem. Phys.* **2018**, *18*, 655–671. [CrossRef]

Publisher's Note: MDPI stays neutral with regard to jurisdictional claims in published maps and institutional affiliations.

© 2020 by the authors. Licensee MDPI, Basel, Switzerland. This article is an open access article distributed under the terms and conditions of the Creative Commons Attribution (CC BY) license (http://creativecommons.org/licenses/by/4.0/).